Structural basis of a two-antibody cocktail exhibiting highly potent and broadly neutralizing activities against SARS-CoV-2 variants including diverse Omicron sublineages

Xiaoman Li[1,*], Yongbing Pan[2,*], Qiangling Yin[3,*], Zejun Wang[2], Sisi Shan[4], Laixing Zhang[1], Jinfang Yu[1], Yuanyuan Qu[5], Lina Sun[3], Fang Gui[2], Jia Lu[2], Zhaofei Jing[2], Wei Wu[3], Tao Huang[3], Xuanling Shi[4], Jiandong Li[3], Xinguo Li[2], Dexin Li[3,6], Shiwen Wang[3,6], Maojun Yang[1], Linqi Zhang[4], Kai Duan[2], Mifang Liang[3,6,#], Xiaoming Yang[2,#], Xinquan Wang[1,#]

Affiliations

[1]The Ministry of Education Key Laboratory of Protein Science, Beijing Advanced Innovation Center for Structural Biology, Beijing Frontier Research Center for Biological Structure, School of Life Sciences, Tsinghua University, Beijing 100084, China.

[2]National Engineering Technology Research Center for Combined Vaccines, Wuhan Institute of Biological Products Co. Ltd., Wuhan 430070, China.

[3]State Key Laboratory for Molecular Virology and Genetic Engineering, National Institute for Viral Disease Control and Prevention, Chinese Center for Disease Control and Prevention, Beijing 102206, China.

[4]NexVac Research Center, Comprehensive AIDS Research Center, Center for Infectious Disease Research, Department of Basic Medical Sciences, School of Medicine, Tsinghua University, Beijing 100084, China.

[5]Institution of Infectious Diseases, Shenzhen Bay Laboratory, Shenzhen 518107, China.

[6]CDC-WIV Joint Research Center for Emerging Diseases and Biosafety, Wuhan 430071, China.

[*]Xiaoman Li, Yongbing Pan, Qiangling Yin contributed equally to this work.

[#]Correspondence Authors:

E-mail address:

liangmf@ivdc.chinacdc.cn (M. Liang); yangxiaoming@sinopharm.com (X. Yang); xinquanwang@mail.tsinghua.edu.cn (X. Wang)

Abstract

SARS-CoV-2 variants of concern (VOCs), especially the latest Omicron, have exhibited severe antibody evasion. Broadly neutralizing antibodies with high potency against Omicron are urgently needed for understanding working mechanisms and developing therapeutic agents. In this study, we characterized previously reported F61, which was isolated from convalescent patients infected with prototype SARS-CoV-2, as a broadly neutralizing antibody against all VOCs including Omicron BA.1, BA.1.1, BA.2, BA.3 and BA.4 sublineages by utilizing antigen binding and cell infection assays. We also identified and characterized another broadly neutralizing antibody D2 with epitope distinct from that of F61. More importantly, we showed that a combination of F61 with D2 exhibited synergy in neutralization and protecting mice from SARS-CoV-2 Delta and Omicron BA.1 variants. Cryo-EM structures of the spike-F61 and spike-D2 binary complexes revealed the distinct epitopes of F61 and D2 at atomic level and the structural basis for neutralization. Cryo-EM structure of the Omicron-spike-F61-D2 ternary complex provides further structural insights into the synergy between F61 and D2. These results collectively indicated F61 and F61-D2 cocktail as promising therapeutic antibodies for combating SARS-CoV-2 variants including diverse Omicron sublineages.

Introduction

Since the first documented cases of the SARS-CoV-2 infection in Wuhan, China in late 2019, the COVID-19 pandemic has been posing a severe threat to the global public health, with more than 523 million infections and over 6 million deaths around the world[1-3] (https://www.who.int/emergencies/diseases/novel-coronavirus-2019/situation-reports/). Vaccines, monoclonal neutralizing antibodies, small-molecule drugs have been successfully developed for prophylaxis and treatment in fighting against the SARS-CoV-2[3-20]. However, SARS-CoV-2 variants, especially variants of concern (VOC) with changed pathogenicity, increased transmissibility and resistance to convalescent/vaccination sera and monoclonal antibodies have emerged repeatedly during the circulation[21-24]. In 2020, the first VOC Alpha (B.1.1.7) was identified in the United Kingdom[25,26], followed by Beta (B.1.351) in South Africa[27] and Gamma (P.1) in Brazil[28]. These three VOCs mainly circulated in their identified and neighboring countries. In contrast, Delta (B.1.617.2) first detected in India in late 2020 quickly spread to nearly all countries and became the global dominant VOC in 2021[29-32]. In November 2021, Omicron (B.1.1.529) was reported from South Africa, and the World Health Organization (WHO) immediately designated it as the fifth VOC due to its over 40 mutations in the spike (S) glycoprotein, at least three times more than the number found in previous four VOCs[33-36]. Although Omicron has lower fatality rate than Delta, it quickly outcompeted Delta and became the dominant circulating variant in 2022, due to the significantly increased transmissibility[33,37]. Currently, the major sublineages of Omicron include BA.1, BA.1.1, BA.2, BA.2.12.1, BA.3, BA.4 and BA.5[38].

The S glycoprotein homotrimer on the surface of SARS-CoV-2 is critical for viral entry by binding cellular receptor ACE2 and mediating fusion of viral and cell membranes[1,39]. The monomeric S glycoprotein consists of the S1 and S2 subunits. The S1 subunit for receptor binding folds into four major domains including the N-terminal domain (NTD), receptor-binding domain (RBD) and two subdomains (SD1 and SD2), while the S2 for membrane fusion has fusion peptide (FP), two heptad repeats (HR1 and HR2) and other secondary structural elements[40]. SARS-CoV-2 neutralizing antibodies bind the S glycoprotein to block its interaction with the ACE2 receptor or interfere with the pre-fusion to post-fusion conformational transition of the S glycoprotein

78 required for membrane fusion[41,42]. Among the domains and secondary structural elements in the S
79 glycoprotein, RBD is the predominant target of neutralizing antibodies that can be grouped into
80 four classes (class 1 to class 4) based on germline or structural information[43]. By including more
81 antibodies and finer epitope binning, the antibody epitopes on the RBD were further redefined into
82 seven core communities (RBD-1 to RBD-7), which are located on the top receptor-binding motif
83 (RBM) face (RBD-1, RBD-2 and RBD-3), the solvent-exposed outer surface (RBD-4 and RBD-5)
84 and the cryptic inner face (RBD-6 and RBD-7) of the RBD[44].

85 Mutations on the RBD play important roles in varied receptor binding and escape of antibody
86 neutralization of SARS-CoV-2 VOCs, thereby affecting viral transmissibility and potency of
87 neutralizing antibodies[29,30,45,46]. Notably, Omicron has close to 20 mutations on the RBD and 10 of
88 them map to the top RBM surface directly interacting with the ACE2 receptor[47,48]. It has been
89 shown that Omicron strikingly reduced or abrogated neutralization titers of sera from vaccinated
90 and convalescent individuals[24,35,49-52]. Most RBD-directed potent antibodies previously identified
91 including those approved for emergency use authorization (EUA) also exhibited markable
92 reduction or complete loss of neutralizing activity against Omicron[24,35,53-56]. For example, a family
93 of class I antibodies using the immunoglobulin heavy chain variable 3-53 or 3-66 gene
94 (IGHV3-53/3-66) strongly bind to the RBM face, and their epitopes are largely within the RBD-2
95 community and overlap with ACE2-binding site. Majority of them are heavily affected by
96 mutations on the RBM face such as Q493R, Q498R, N501Y and Y505H[43,48,53,56]. Similarly,
97 N440K, G446S and E484A mutations found on the Omicron RBD are involved in reducing the
98 activities of the class 2 and class 3 antibodies targeting RBD-4 and RBD-5 on the outer surface,
99 while S371L, S373P and S375F heavily affect many antibodies in the class 4 targeting RBD-6 and
100 RBD-7 on the inner surface[48,53,56].

101 Previously we reported a neutralizing antibody F61 from convalescent patients after
102 prototype SARS-CoV-2 infection, which showed high potency in neutralizing SARS-CoV-2 and
103 Alpha, Beta and Delta variants[57]. In this study, we showed that F61 using the IGHV3-53/3-66
104 gene exhibited the same high potency in neutralizing Omicron diverse sublineages and protecting
105 mouse model against Delta and Omicron BA.1 variants. Therefore, F61 is an exceptional broadly
106 neutralizing antibody in the family of IGHV3-53/3-66-using antibodies. We also reported another

107 broadly neutralizing antibody D2 that is able to potently neutralize SARS-CoV-2 VOCs except
108 Omicron BA.1.1 and BA.4, although its potency is less than that of F61. More importantly, we
109 showed that F61 and D2 exhibited significant synergy in both in vitro neutralization of all VOCs
110 and in vivo protection against Delta and Omicron BA.1. Cryo-EM structure determination of the
111 spike-Fab complexes revealed the distinct epitopes of F61 and D2 on the RBD and provided
112 structural insights into the broad and potent neutralization by F61 and F61-D2 cocktail against all
113 SARS-CoV-2 VOCs including diverse Omicron sublineages.
114

115 **Results**

116 **Biochemical characterization of neutralizing antibodies F61 and D2**

117 We previously reported a phage-displayed antibody library constructed from the PBMCs of
118 SARS-CoV-2 convalescent donors[57]. Both F61 and D2 were isolated by screening this library with
119 wildtype SARS-CoV-2 RBD (WT-RBD). After purifying these two antibodies in the recombinant
120 form of human IgG1, we tested their binding avidity to different fragments of the WT, Delta and
121 Omicron spike glycoproteins using ELISA method. These fragments include WT-S1, WT-NTD,
122 WT-RBD, Delta-S1, Delta-RBD and Omicron-RBD (BA.1). The ELISA results showed that F61
123 and D2 bound to above fragments but not WT-NTD with EC50 values less than 4.5 ng/mL (Fig.
124 1A), indicating that they are both RBD specific antibodies.

125 We also measured the binding affinities of F61 and D2 to Delta-RBD and Omicron-RBD
126 (BA.1 and BA.2) using surface plasmon resonance (SPR) method (Fig. 1B and Fig. S1). Both
127 antibodies exhibited high-affinity binding to Delta-RBD, Omicron-RBD-BA.1 and
128 Omicron-RBD-BA.2. The K_D values to Delta-RBD, Omicron-RBD-BA.1 and
129 Omicron-RBD-BA.2 by F61 were ~3.89 pM, ~5.03 nM and ~93.3 pM, respectively. We
130 previously reported the K_D of ~3.72 pM to the WT-RBD[57]. Therefore, the binding of F61 to
131 WT-RBD and Delta-RBD are on the same level. Its binding to Omicron-RBD was reduced by
132 ~1000-fold for BA.1 (K_D = ~5.03 nM) and ~30-fold for BA.2 (K_D = ~93.3 pM). D2 retained
133 high-affinity binding on pM level to Delta-RBD (K_D = ~62 pM), Omicron-RBD-BA.1 (K_D =
134 ~5.45 pM) and Omicron-RBD-BA.2 (K_D = ~5.22 pM), and the binding to Delta-RBD is slightly
135 weaker than that to Omicron-RBD. Next, we examined the effects of these two antibodies in

136 inhibiting the staining of hACE2-expressing HEK293 cells by WT-RBD-mFC fusion protein using
137 FACS (Fig. 1C). The results showed that F61 not D2 was able to compete with ACE2 receptor in
138 binding WT-RBD, indicating their distinct binding epitopes on the RBD.
139
140 **Broadly neutralizing activities of F61 and F61-D2 cocktail against SARS-CoV-2 VOCs in**
141 **vitro and in vivo**
142 We tested the neutralizing activities of F61 and D2 against pseudoviruses of SARS-CoV-2 WT
143 (D614G) and its VOCs including Alpha (B.1.1.7), Beta (B.1.351), Delta (B.1.617.2 and B.1.617.3)
144 and Omicron (BA.1, BA.1.1, BA.2, BA.3 and BA.4) (Fig. 2A). Corresponding to the high-affinity
145 binding, F61 was highly potent in neutralizing SARS-CoV-2 WT pseudovirus with half-maximal
146 inhibitory concentration (IC50) of 6 ng/mL. All IC50 values against the tested VOCs were less
147 than 20 ng/mL (Fig. 2A). These results showed that F61 exhibited high potency and broad
148 neutralization against Alpha, Beta, Delta and Omicron, even its binding to Omicron-RBD-BA.1
149 was significantly reduced (~1000-fold) compared to WT-RBD (Fig. 1B). Similar to F61, D2 was
150 able to potently neutralize SARS-CoV-2 WT pseudovirus with IC50 of 19 ng/mL, and it retained
151 the same level high potencies in neutralizing pseudoviruses of Alpha, Beta, Delta and Omicron
152 including BA.1, BA.2 and BA.3 with IC50 values less than 50 ng/mL (Fig.2A). However, its
153 potency against pseudovirus of Omicron BA.1.1 and BA.4 was reduced with IC50 values
154 increased to 249 and 318 ng/mL, respectively (Fig. 2A). Considering distinct epitopes of F61 and
155 D2 indicated by the competition assay, we also tested the combination of F61 and D2 with a 1:1
156 molar ratio in pseudovirus neutralization. The results showed that all tested VOCs were well
157 neutralized with IC50 values less than 30 ng/mL by using the F61-D2 cocktail (Fig. 2A).
158 Next, we studied the neutralization of authentic SARS-CoV-2, Delta B.1.617.2 and Omicron
159 BA.1, BA1.1 and BA.2 by F61 and D2. F61 had IC50 values of 50, 10, 160, 200 and 130 ng/mL
160 against SARS-CoV-2, Delta, Omicron BA.1, Omicron BA.1.1 and Omicron BA.2, respectively
161 (Fig. 2B). By increasing the IC50 value from 50 ng/mL against SARS-CoV-2 to more than 100
162 ng/mL against Omicron BA.1, BA.1.1 and BA.2 (Fig. 2B), the effects of Omicron mutations in
163 reducing F61 potency were more obvious in neutralizing authentic viruses than pseudoviruses.
164 The D2 exhibited less potency than F61, with the IC50 values against SARS-CoV-2, Delta

165 B.1.617.2, Omicron BA.1 and BA.2 were 140, 390, 350 and 162 ng/mL, respectively (Fig. 2B). In
166 consistent with reduced activity against Omicron BA.1.1 pseudovirus, its potency against the
167 authentic Omicron BA.1.1 was also significantly impaired with IC50 value of more than 800
168 ng/mL (Fig. 2B). We further tested the F61-D2 cocktail and the results indicated a synergy
169 between them in the neutralization, especially against Omicron BA.1, BA.1.1 and BA.2. When
170 neutralizing these three Omicron sublineages, F61 and D2 together with a 1:1 molar ratio showed
171 a 1.5 to 6.1-fold improvement in IC50 values over the individual antibodies (Fig. 2B), suggesting
172 an effect that is more than an additive for the F61-D2 cocktail against SARS-CoV-2 and its
173 variants.

174 Finally, using K18-hACE2 mice as a prophylactic model as previously described[58], in vivo
175 protective activities of F61, D2 and F61-D2 cocktail were evaluated with the lethal challenge of
176 Delta and Omicron BA.1 viruses, respectively (Fig. 2C). The results showed that, regardless of
177 giving a high dose (20 mg/kg body weight) or low dose (5 mg/kg or 1.25 mg/kg body weight) of
178 F61, D2 or F61-D2 combination, the antibody treatment conferred protection against the lethal
179 challenges with 100 $TCID_{50}$ Delta or 200 $TCID_{50}$ Omicron BA.1 (Fig. 2C, left panel). Most of
180 tested mice in the experimental end-point did not lose their body weight significantly, in particular
181 with Omicron BA.1 challenge (Fig. 2C, middle panel). Moreover, the viral RNAs in the lung of
182 mice of F61 or F61-D2 cocktail groups were significantly reduced or negatively detected
183 compared with PBS groups (10^8 copies/mL for both Delta or Omicron BA.1), whereas the
184 decrease in viral load in the D2 group was not as significant as in the F61 group (Fig. 2C, right
185 panel). More importantly, the significant synergy between F61 and D2 was also observed in vivo
186 with the lethal challenge of either Delta or Omicron BA.1, even at the minimum administration
187 dose of 1.25 mg/kg body weight, the viral loads in related mice lung were negative or below the
188 minimum detection limit (less than 10^5 copies/mL) (Fig. 2C, right panel).

189

190 **Overall cryo-EM structures of the spike-antibody complexes**

191 To understand structural basis for the binding and neutralization by F61 and D2, we expressed and
192 produced the six proline-stabilized (S6P) WT spike ectodomain with S1/S2 furin-cleavage site
193 mutated to GSAS. The complexes of the WT-spike bound by F61 or D2 Fab were prepared and

194 single particle cryo-EM data were collected, resulting in the binary WT-spike-F61 and
195 WT-spike-D2 structures determined at 3.62 and 3.25 Å, respectively (Fig. S2-S4 and Table S1).
196 We also prepared the Omicron BA.1 spike ectodomain with S6P and GSAS mutations and
197 determined the cryo-EM structure of the ternary Omicron-spike-F61-D2 complex at a resolution
198 of 3.04 Å (Fig. S2-S4 and Table S1). Due to the conformational heterogeneity of the Fab-bound
199 RBDs relative the rest of the spike trimer, only the VH and VL domains of the bound Fab were
200 built in all final models.

201 It has been found that the apo SARS-CoV-2 spike trimer usually exhibits a mixture of a
202 closed form with all three RBDs in the down position and an open form with one RBD in the up
203 position[40,59,60]. In the binary spike-F61 and spike-D2 complexes, the spike trimer is in the open
204 form with all three RBDs adopting similar upright position with a tilt angle of ~90 degree (Fig. 3A
205 and 3B). In the spike-F61 complex, each up-RBD was bound by a F61 Fab on the top
206 receptor-binding motif (RBM) surface for ACE2 engagement (Fig. 3A). Among seventeen RBD
207 residues involved in ACE2 binding, ten of them were recognized by F61, resulting in a large
208 overlap between F61 epitope and ACE2 binding site (Fig. 3D). In the spike-D2 complex, each
209 up-RBD was bound by a D2 Fab covering the solvent-exposed outer surface (Fig. 3B), resulting in
210 an epitope on the RBD spatially distinct from ACE2 binding site (Fig. 3D). In the determined
211 Omicron-spike-F61-D2 ternary complex structure, three RBDs are all in the up position, and each
212 up-RBD was bound simultaneously by one F61 Fab and one D2 Fab (Fig. 3C and 3D).

213

214 **Structural basis for the potent and broad neutralization**

215 We performed focused 3D classification and local refinement of the Fab-RBD region, resulting in
216 improved densities for building the WT-RBD/Fab and Omicron-RBD-BA.1/Fab interfaces (Fig.
217 S4). We utilized the Omicron-RBD-BA.1/Fab interfaces for the following structural description
218 and analysis, due to their better densities compared to WT-RBD/Fab interfaces. F61 using
219 IGHV3-66 gene is a member of the class 1 antibody, and it binds to an epitope on the RBM face
220 that can be grouped into the RBD-2a community[43,44] (Fig. 4A). The interaction buried a total of
221 1145 $Å^2$ surface area from F61 and 1075 $Å^2$ from RBD. All six CDRs of F61 are involved in RBD
222 binding (Fig. 4A), and the heavy chain is more dominant than the light chain by contributing 19

223 residues among all 26 antibody residues for binding (Table S2). The F61 epitope consisting of 25
224 RBD residues does not include Alpha mutation and includes Beta K417N and Delta T478K
225 substitutions. Omicron has more mutations in the F61 epitope, including K417N, S477N, T478K,
226 Q493R and Y505H for BA.1 and BA.1.1. F61 epitope includes additional mutation sites found in
227 other Omicron sublineages, which are D405N and R408S on BA.2, D405N on BA.3 and D405N,
228 R408S and F486V on BA.4 and BA.5 (Fig. 4A and 4C). At the Omicron-RBD-BA.1/F61 interface,
229 N417, N477, K478, R493 and H505 have extensive interactions with F61 residues E26, I28, Y33,
230 Y99, D101 and F102 from the heavy chain, and N31 and D51 from the light chain (Fig. 4C).
231 Therefore, these Omicron mutations work in concert to alter specific interactions at the interface
232 and significantly reduced the binding of F61 to Omicron-RBD-BA.1 (K_D = ~5.03 nM) compared
233 to WT-RBD (K_D = ~3.89 pM) (Fig. 1B). Compared to Omicron-RBD-BA.1, the binding of
234 Omicron-RBD-BA.2 to F61 was restored to some extent with the K_D value of ~93.3 pM (Fig. 1B),
235 indicating that the additional D405N and R408S mutations on Omicron BA.2 would play roles in
236 enhancing the binding by F61. To be note, even for Omicron-RBD-BA.1 whose binding by F61
237 was the most significantly reduced (~1000-fold), the affinity between them is still in low nM
238 range (~5.03 nM). We conclude that the tight binding and direct ACE2 competition would allow
239 for the high potency and broad neutralization of F61 to be retained against SARS-CoV-2 VOCs
240 including diverse Omicron sublineages.

241 Structure determination showed that the epitope D2 using IGHV3-9 gene is on the outer
242 surface of the RBD, locating between previously defined RBD-4 and RBD-5 communities and
243 having overlap with both of them[43,44] (Fig. 4B). Upon binding, the VH domain of D2 contacts the
244 up-RBD by aligning in parallel with the outer surface, whereas the VL domain does not have
245 contact with the RBD (Fig. 4B). The interaction between D2 VH domain and up-RBD buried a
246 total of 953 $Å^2$ surface area from the VH domain and 944 $Å^2$ from the RBD. At the interface, 11
247 residues from the D2 heavy chain HCDR2 and HCDR3 interact with 13 Omicron-RBD residues
248 (Fig. 4B and Table S2). Among close to 20 mutations on the Omicron-RBD, the D2 epitope
249 include only G446S mutation found on BA.1 but not on BA.2 (Fig. 4D). The interaction around
250 S446 at the Omicron-RBD-BA.1/D2 interface is between heavy chain K65 and the main-chain
251 oxygen atom of S446 (Fig. 4D), which could explain that the binding of D2 to Omicron-RBD

252 BA.1 or BA.2 was retained on pM level and D2 could still potently neutralize Omicron BA.1 and
253 BA.2 (Fig. 1B, Fig. 2A and 2B). D2 epitope includes G446S and R346K mutation sites on BA.1.1
254 and only L452R on BA.4 and BA.5 (Fig. 4B & 4D). R346 has extensive interactions with D2
255 residues D52, N54, G56, V57, I58, E103 and S104, including hydrogen bonds of R346 with D52,
256 N54, E103 and S104 and salt bridge of R346 with D52 (Fig. 4D). R346K substitution is expected
257 to abolish some hydrogen bonds and to interfere with interactions around the 346 between
258 Omicron BA.1.1 RBD and D2, resulting in reduced neutralization against Omicron BA.1.1
259 compared to BA.1, BA.2 and BA.3 (Fig. 2A and 2B). L452 has hydrophobic interaction with D2
260 heavy chain I69 (Fig. 4D). Similar to R346K mutation, the L452R mutation found in Omicron
261 BA.4 would also interfere local interactions and result in reduced neutralization against BA.4
262 compared to BA.1, BA.2 and BA.3 (Fig. 2A and 2B).
263
264 **Discussion**
265 A large number of potent neutralizing antibodies against SARS-CoV-2 have been reported since
266 the beginning of the COVID-19 pandemic[4,6-9,13,14,20]. However, the emergence of SARS-CoV-2
267 VOCs harboring mutations on the spike glycoprotein has led to great concerns over resistance to
268 neutralizing antibodies and failure of vaccines[23,24,30,35,49-56,61]. In fact, recent studies have found that
269 most of previously identified neutralizing antibodies have shown markable reduction or complete
270 loss of activities against Omicron[24,35,53-56]. Here we comprehensively characterized a highly potent
271 and broadly neutralizing antibody F61 and its cocktail with another antibody D2 against
272 SARS-CoV-2 VOCs including Omicron.
273 The IGHV3-53/3-66-using antibodies are frequently elicited in most people after
274 SARS-CoV-2 infection or vaccination and many of them exhibit high potency by strongly binding
275 to the RBM and directly competing with ACE2 receptor[62]. However, most of them are heavily
276 affected by VOCs, especially Omicron carrying multiple mutations on the RBM[24,53-56,63].
277 Previously we showed that F61 was highly potent against SARS-CoV-2 WT and Alpha, Beta and
278 Delta variants in pseudovirus inhibition[57]. Here we showed that F61 was still highly potent against
279 Omicron BA.1, BA.1.1, BA.2 BA.3 and BA.4 pseudoviruses with IC50 values below 20 ng/mL. It
280 was able to neutralize cell infection of authentic Omicron BA.1, BA.1.1 and BA.2 with IC50

281 values below 200 ng/mL, respectively. Structure of Omicron-RBD-BA.1/F61 interface indicated
282 that despite close to twenty mutations in Omicron-RBD-BA.1, F61 could still interact with these
283 residues, such as N417, N477, K478, R493 and H505. Furthermore, F61 also formed salt bridges
284 with R493 and hydrogen bonds with N417 and H505. Given that neutralization titers of many
285 monoclonal antibodies and sera from vaccinated and convalescent individuals are significantly
286 reduced because of K417N, Q493R and Y505H mutations, robust binding with these mutation
287 sites by F61 may explain why it stands out from other antibodies and shows excellent
288 neutralization against all tested variants, including Omicron BA.1, BA.1.1, BA.2, BA.3 and BA.4
289 sublineages. These results collectively showed that F61 is an exceptional IGHV3-53/3-66-using
290 antibody exhibiting potent and broadly neutralizing activity. CAB-A17 is another recently
291 reported IGHV3-53/3-66-using antibody with broad neutralizing activity[64]. CAB-A17 and F61
292 exhibited similar high potency against Omicron pseudovirus (CAB-A17 IC50: ~15 ng/mL; F61
293 IC50: 10-20 ng/mL)[64]. Structure and sequence comparisons showed that the Omicron-RBD
294 epitope residues are nearly the identical, and antibody residues involved in hydrogen-bonding
295 interaction are also highly conserved between CAB-A17 and F61, such as heavy chain E26, Y33,
296 G54, S56 and R97[64]. The study of CAB-A17 also found that only four somatic hypermutations
297 G26E, T28I, S53P and Y58F were able to confer breadth to CAB-A17 to against Omicron[64], and
298 E26, I28, P53 and F58 are also conserved in F61. To be note, F61 and CAB-A17 are two
299 significant examples of VOC-neutralizing antibodies isolated from convalescent patients before
300 circulation of VOCs, indicating that broadly neutralizing antibodies are within the repertoire after
301 prototype SARS-CoV-2 infection and such memory B cells could be recruited upon re-infection or
302 vaccination.

303 Here we also reported another broadly neutralizing antibody D2, although its potency is
304 weaker than that of F61. Structural elucidation of the RBD/D2 interfaces confirmed that the
305 epitope of D2 is relatively conserved and almost unchanged in tested VOCs, and thus it is
306 unaffected by most VOCs. It only includes G446S mutation in Omicron BA.1, BA.2 and BA.3
307 and our structure shows that D2 remains interaction with Omicron BA.1 S446. However, RBD
308 residue R346 is within the epitope and has extensive interactions with D2, which may
309 dramatically reduce its neutralization activity against Omicron BA.1.1. These structural

310 observations fit well with functional data showing that D2 broadly bound and neutralized Omicron
311 BA.1, BA.2 and BA.3 and its potency was significantly reduced against Omicron BA.1.1 carrying
312 the R346K mutation. Although RBD-directed SARS-CoV-2 neutralizing antibodies have been
313 extensively studied and summarized such as the class 1-4 antibody and RBD1-7 communities[43,44],
314 the overall binding mode and epitope of D2 are still out of ordinary. Its epitope is between RBD-4
315 and RBD-5 and overlaps with both of them. Therefore, unlike many class 2 antibodies having
316 RBD-4 epitope, D2 does not compete with ACE2 and its epitope does not include E484K/A
317 mutation that reduces or abolishes the neutralizing activity of many antibodies in the RBD-4
318 community[53,54,56]. At the same time, unlike many class 3 antibodies having RBD-5 epitope, D2
319 does not bind to the N343-linked glycans centered in RBD-5 epitope, which is highly conserved
320 among SARS-CoV-2, SARS-CoV-1 and many bat and pangolin betacoronaviruses[14,44,65].
321 Structural comparison showed that D2 is similar to a recently reported antibody COVOX-58 in
322 overall binding mode and epitope on the RBD[61] (Fig. S5). These two antibodies use the same
323 IGHV3-9 gene. Although the HCDR3 of COVOX-58 is longer than that of D2, their epitopes on
324 the RBD are very similar due to the dominant role of the conserved HCDR2 in RBD binding by
325 F61 and COVOX-58[61] (Fig. S5).

326 We also proved that F61 and D2 exhibited significant synergy both in vitro and in vivo.
327 Animal experiments showed that F61-D2 cocktail could provide protection against Delta and
328 Omicron BA.1. Even when mice were administrated at the minimum dose of 1.25 mg/kg body
329 weight, the viral loads in their lung were still negative or below the minimum detection limit.
330 These in vivo experiments implicate that F61-D2 cocktail could be a promising therapeutic
331 combination for combating SARS-CoV-2 variants of concern, including Omicron. We aligned
332 RBD-F61 or RBD-D2 binary complexes onto the spike trimers in the closed form or in the open
333 form with one or two RBDs adopting the up conformation. The results showed that F61 and D2
334 epitopes are only fully exposed in the up-RBD (Fig. S6), indicating that the down to up
335 conformational change is a prerequisite for the binding of F61 and D2. After binding to the RBM
336 face, one important mechanism of F61 neutralization is to directly block spike-ACE2 interaction.
337 The major neutralizing mechanism of D2 would not be ACE2 competition because its epitope
338 does not overlap with ACE2-binding site. The destabilization of spike trimer by representative

class 3 antibody S309 was suggested to be its mechanism of action[48], and D2 may utilize similar working mechanism. Due to the distinct epitopes, when F61 and D2 are used as a cocktail, one antibody binding to the RBD may help to induce and fix the RBD in the up conformation for efficient binding of the other antibody. In this way, the F61-D2 cocktail would be more efficient than individual F61 in fully binding the spike trimer and blocking all ACE2-binding sites, as shown in the Omicron-RBD-F61-D2 ternary complex structure (Fig. 3C).

346 **Figures and Figure legends**

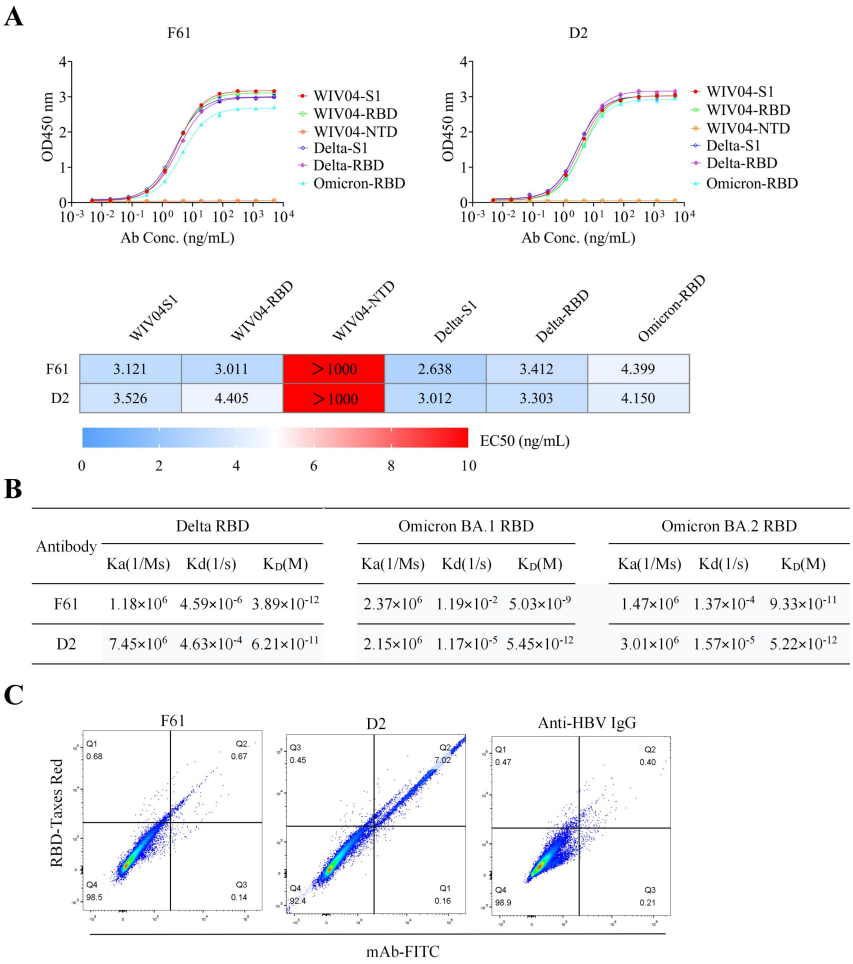

	WIV04S1	WIV04-RBD	WIV04-NTD	Delta-S1	Delta-RBD	Omicron-RBD
F61	3.121	3.011	>1000	2.638	3.412	4.399
D2	3.526	4.405	>1000	3.012	3.303	4.150

Antibody	Delta RBD			Omicron BA.1 RBD			Omicron BA.2 RBD		
	Ka(1/Ms)	Kd(1/s)	K_D(M)	Ka(1/Ms)	Kd(1/s)	K_D(M)	Ka(1/Ms)	Kd(1/s)	K_D(M)
F61	1.18×10^{6}	4.59×10^{-6}	3.89×10^{-12}	2.37×10^{6}	1.19×10^{-2}	5.03×10^{-9}	1.47×10^{6}	1.37×10^{-4}	9.33×10^{-11}
D2	7.45×10^{6}	4.63×10^{-4}	6.21×10^{-11}	2.15×10^{6}	1.17×10^{-5}	5.45×10^{-12}	3.01×10^{6}	1.57×10^{-5}	5.22×10^{-12}

347

348 **Fig. 1 Biochemical characterization of neutralizing antibodies F61 and D2. A,** Binding
349 profiles of mAbs measured by ELISA. **B,** Binding kinetics of mAbs with Delta-RBD,
350 Omicron-RBD (BA.1 and BA.2) measured by SPR. **C,** Antibody and ACE2 competition for
351 binding to SARS-CoV-2 WT-RBD measured by FACS.

352

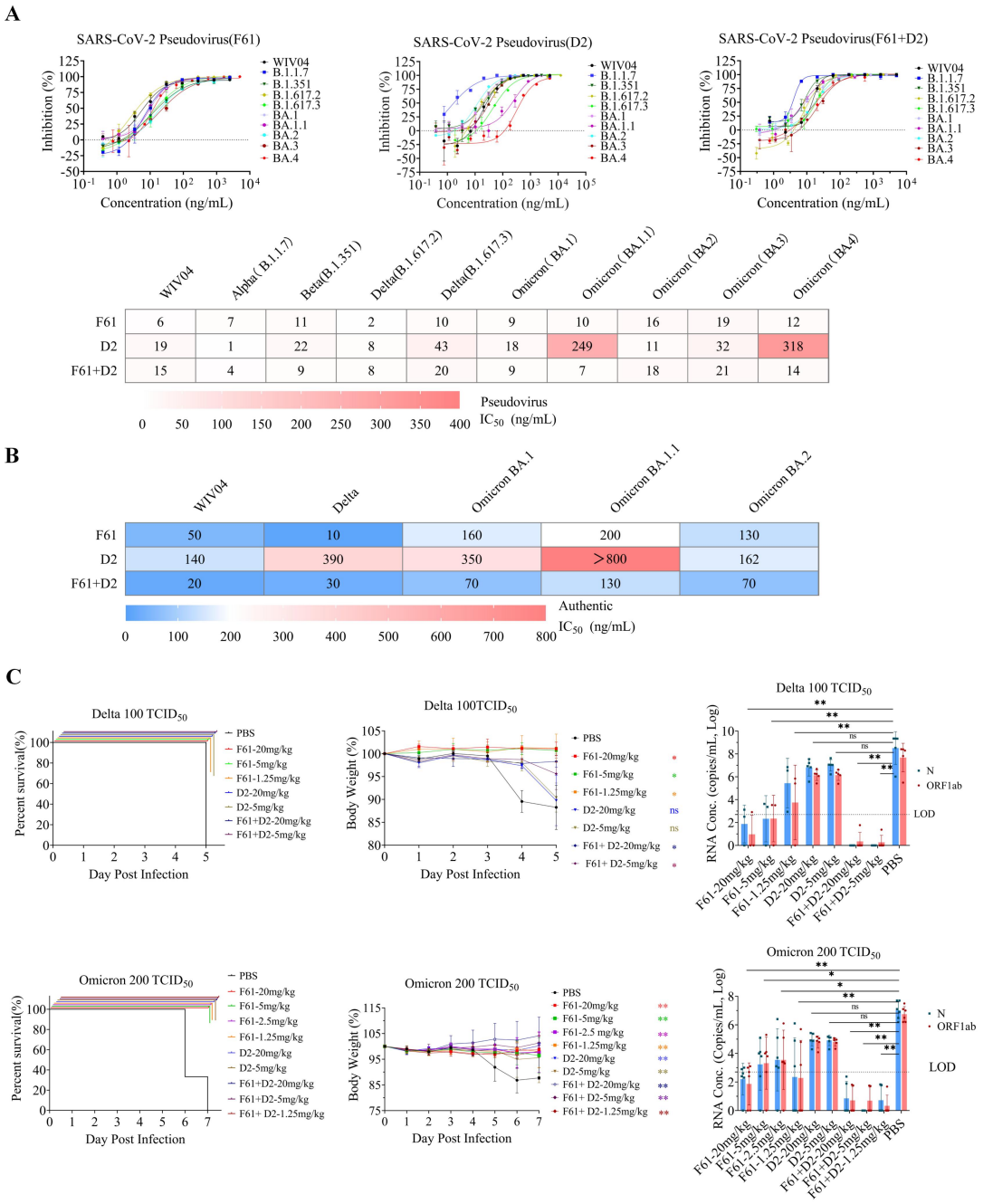

Fig. 2 Broadly neutralizing activities of F61 and F61-D2 cocktail against SARS-CoV-2 VOCs in vitro and in vivo. A, Neutralization of mAbs to SARS-CoV-2 pseudovirus in HEK293T-hACE2 cells. **B,** Neutralization of mAbs to SARS-CoV-2 authentic virus in Vero E6 cells. **C,** Prophylactic effects of F61, D2 or F61-D2 cocktail against SARS-CoV-2 Omicron BA.1 and Delta variants in K18-hACE2 mice. Body weights change (%), survival curves, and viral RNA loads in the lungs of K18-hACE2 mice treated with difference doses of antibodies (1.25, 2.5, 5, 20 mg/kg) F61, D2, or F61+D2 via intranasal route before infection with 100 $TCID_{50}$/mouse

361 Delta variant (**upper panel**) or 200 $TCID_{50}$/mouse Omicron BA.1 variant (**down panel**). As a
362 negative control, PBS was administered. Body weight curve values represent means ± standard
363 errors of the means (n = 4~6 mice/group). Significant differences between the antibody treatment
364 group and negative control are shown. All data points for viral load in the lungs are shown, along
365 with the medians. ns, $P > 0.05$; *, $P < 0.05$; **, $P < 0.0001$, as determined by One -way ANONA.
366 Limit of detection (LOD), 500 copies/mL.
367

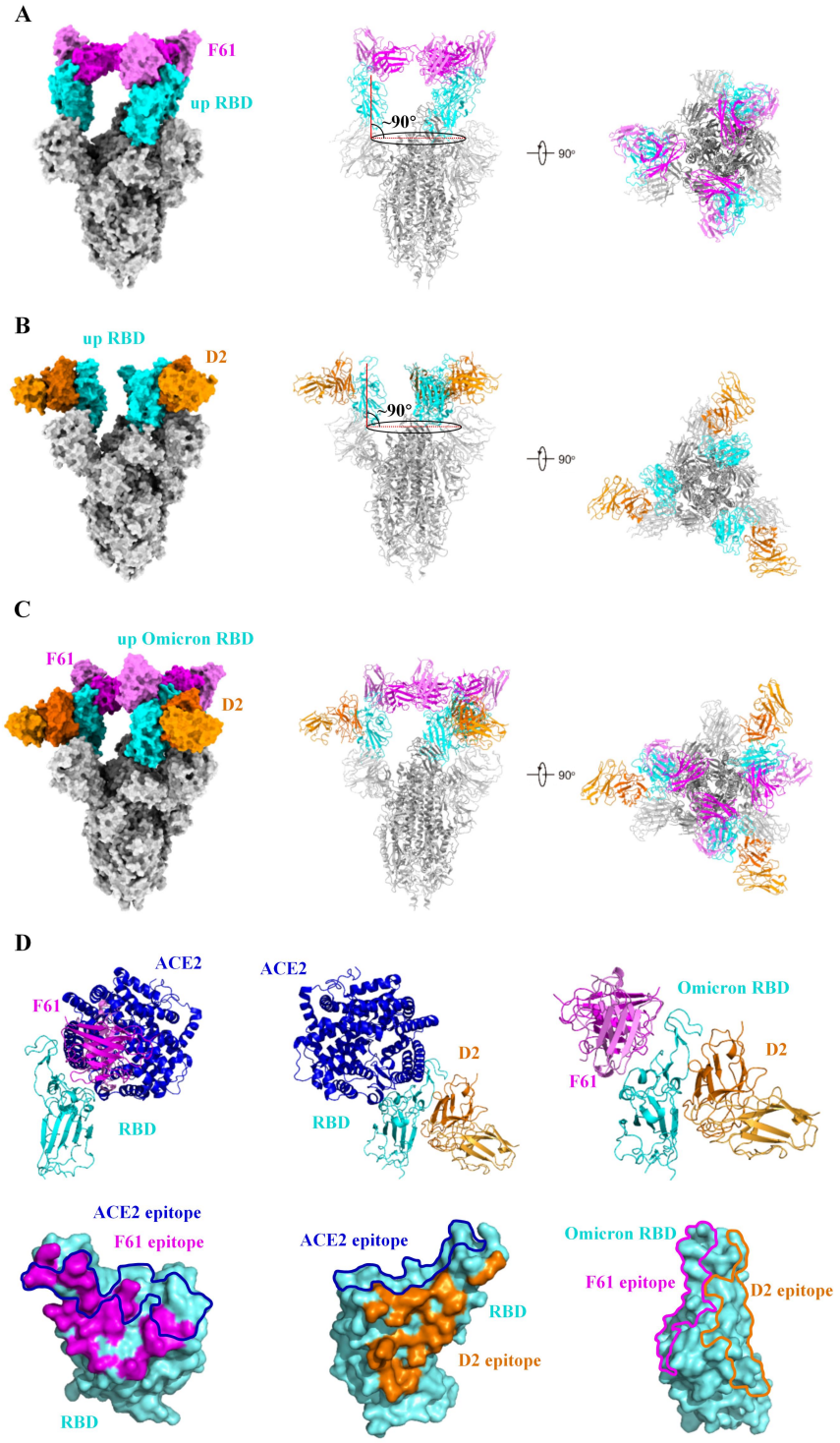

Fig. 3 Overall cryo-EM structures of the spike-antibody complexes. A, Overall structure of SARS-CoV-2 spike in complex with F61 Fab. The tilt angle of RBD is defined by the angle between the long axis of RBD (red line) and its projection on the horizontal plane (black ellipse). Angle between them is indicated. SARS-CoV-2 RBD is colored in cyan, other domains in grey, heavy chain of F61 in magenta and light chain of F61 in violet. **B,** Overall structure of

374 SARS-CoV-2 spike in complex with D2 Fab. The tilt angle of RBD is defined by the angle
375 between the long axis of RBD (red line) and its projection on the horizontal plane (black ellipse).
376 Angle between them is indicated. SARS-CoV-2 RBD is colored in cyan, other domains in grey,
377 heavy chain of D2 in orange and light chain of D2 in light orange. **C,** Overall structures of
378 SARS-CoV-2 Omicron spike in complex with F61 Fab and D2 Fab. Color schemes are the same
379 as **A** and **B**. **D,** Structural superposition of RBD-fab and RBD-ACE2 (PDB ID: 6M0J) structures
380 and the footprints of F61, D2 and ACE2 on the RBD, and structure of Omicron-RBD-F61-D2 with
381 footprints of F61 and D2 on the RBD. ACE2 is colored in blue. The footprints of F61, D2 and
382 ACE2 are represented as magenta, orange and blue, respectively. Other color schemes are the
383 same as **A** and **B**.
384

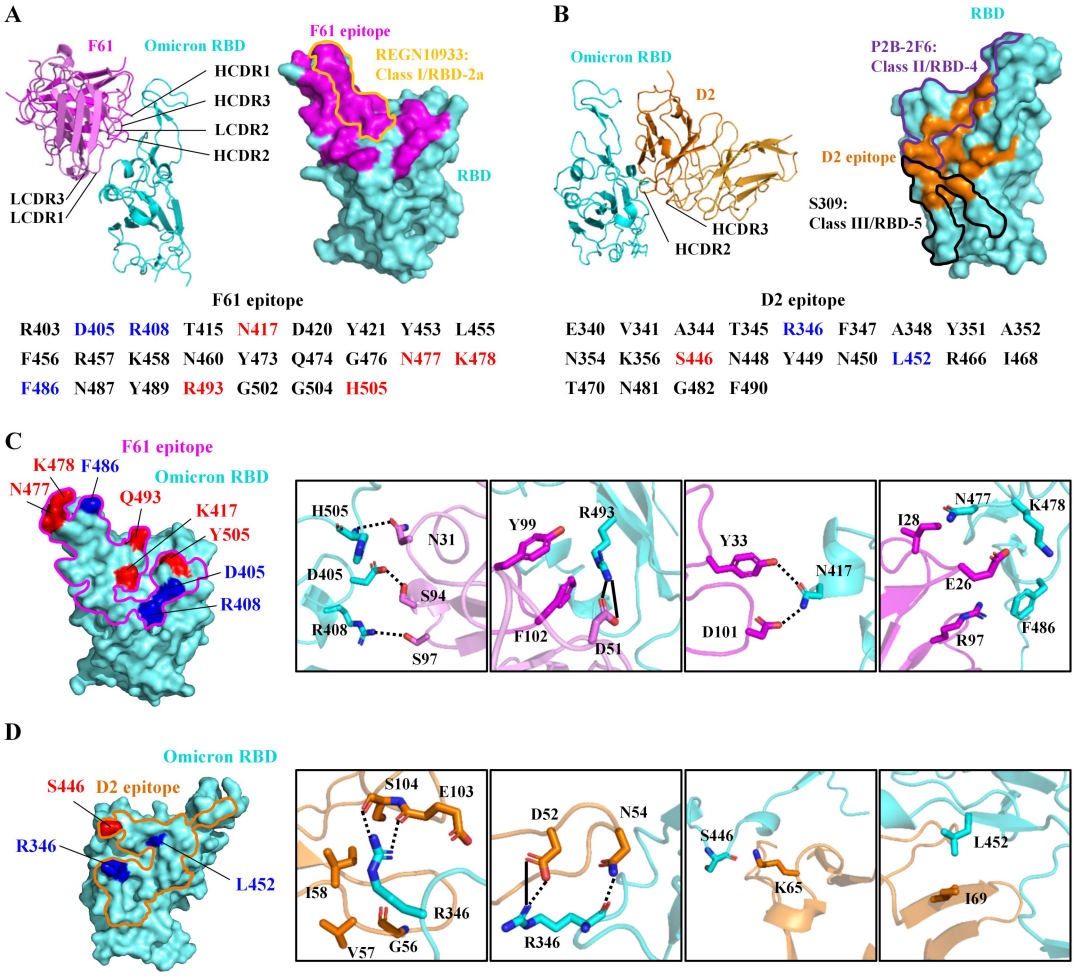

Fig. 4 Structural basis for the potent and broad neutralization. A, Overall structure of Omicron-RBD-BA.1 bound with F61 and CDRs involved in binding are labeled. On the RBD, the footprints of F61 is represented by magenta surface and the footprint of REGN10933 (PDB ID: 6XDG) is circled by yellow line. Omicron-RBD-BA.1 residues recognized by F61 are listed and mutated N417, N477, K478, R493 and H505 in BA.1 are colored red. Additional mutations sites in BA.2 (D405 and R408), BA.3 (D405), BA.4 (D405, R408 and F486) and BA.5 (D405, R408 and F486) are colored blue. **B,** Overall structure of Omicron-RBD- BA.1 bound with D2 and CDRs involved in binding are labeled. On the RBD, the footprint of D2 is represented by orange surface and the footprints of P2B-2F6 (PDB ID: 7BWJ) and S309 (PDB ID: 6WPS) are circled by purple and black lines, respectively. Omicron-RBD-BA.1 residues recognized by D2 are listed and mutated S446 in BA.1 is colored red. Additional mutation site in BA.1.1 (R346) and only L452 mutation site in BA.4 and BA.5 are colored blue. **C,** The detailed interactions between residues mutated in above Omicron sublineages and F61. F61 footprint is circled by a magenta line.

Interacting residues of Omicron-RBD are shown as cyan sticks and F61 are shown as magenta sticks. Hydrogen bonds and salt bridges are represented by dashed lines and solid lines, respectively. **D,** The detailed interactions between residues mutated in above Omicron sublineages and D2. D2 footprint is circled by an orange line. Interacting residues of Omicron-RBD are shown as cyan sticks and D2 are shown as orange sticks. Hydrogen bonds and salt bridges are represented by dashed lines and solid lines, respectively.

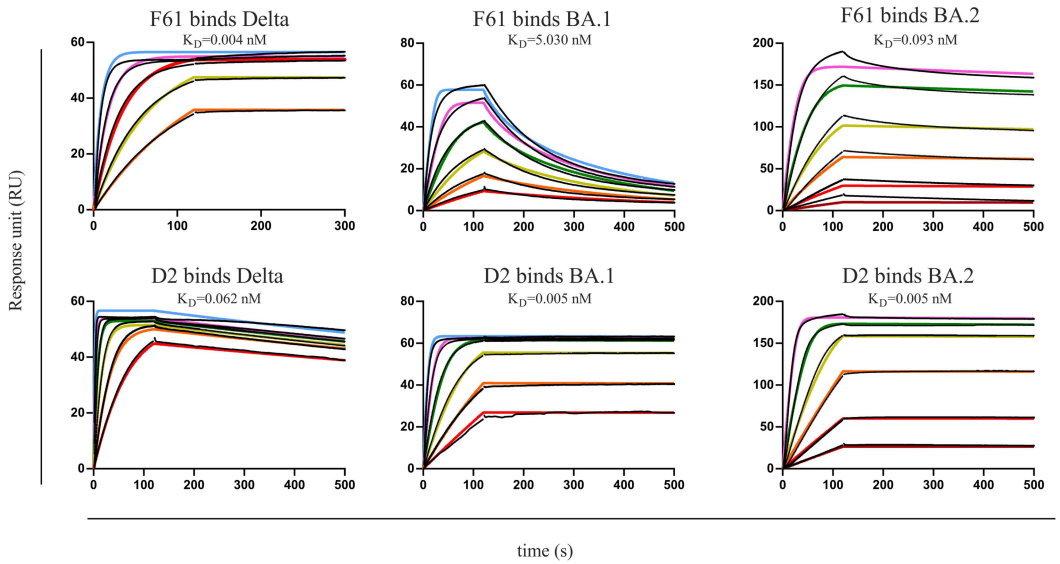

Fig. S1. The binding curves between mAbs and SARS-CoV-2 Delta or Omicron RBD measured by SPR. Black lines were the original curves, while colored lines were the fitted curves.

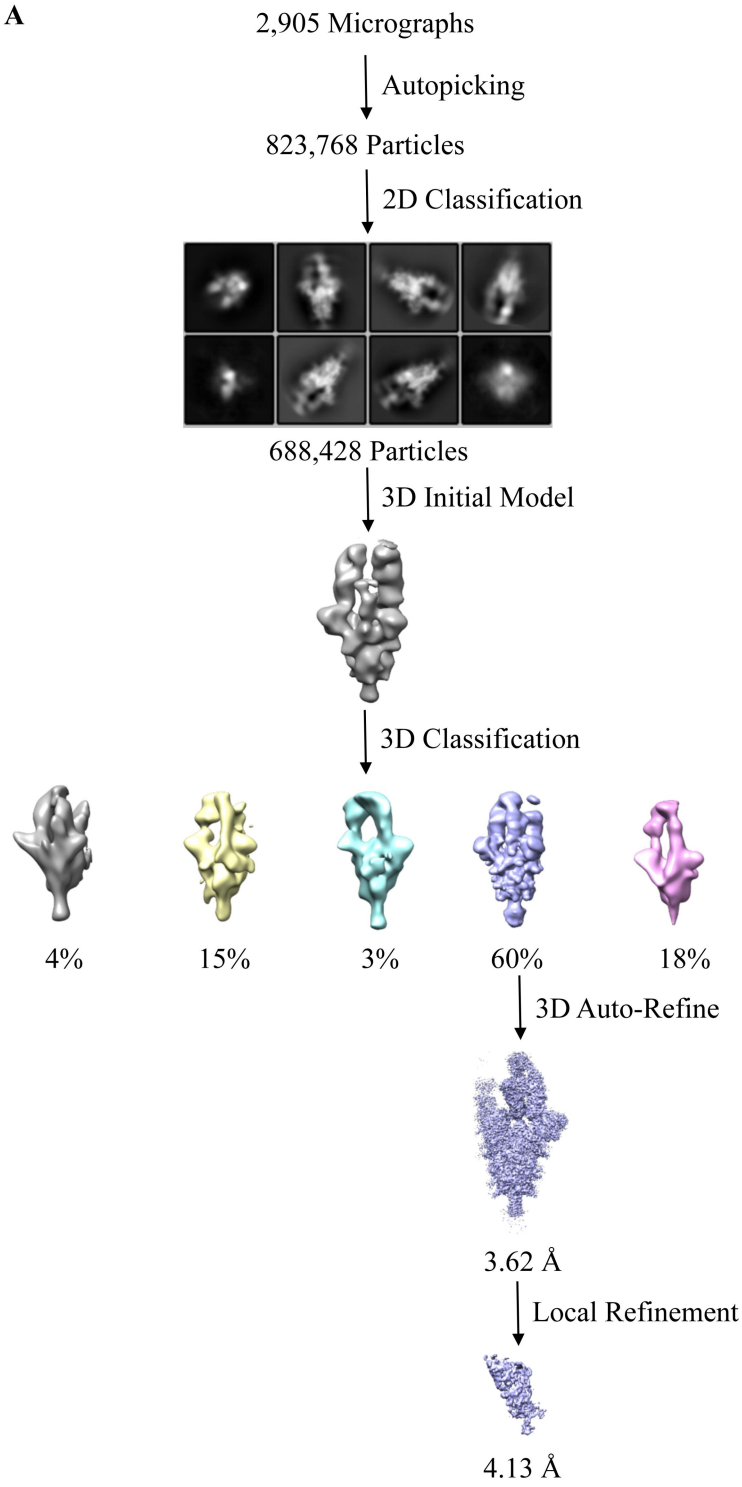
A
2,905 Micrographs
Autopicking
823,768 Particles
2D Classification
688,428 Particles
3D Initial Model
3D Classification
4%
15%
3%
60%
18%
3D Auto-Refine
3.62 Å
Local Refinement
4.13 Å

411

B

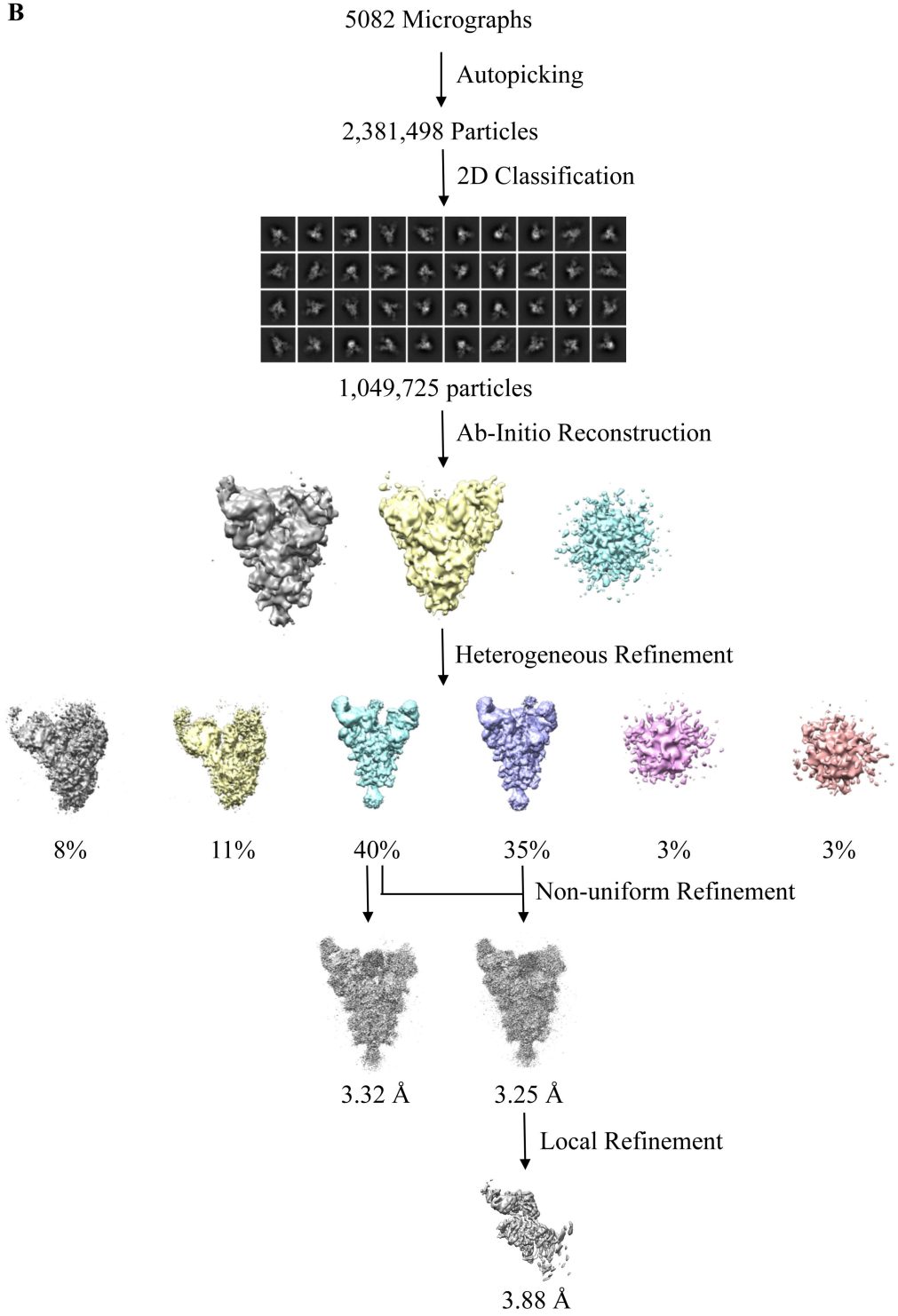
5082 Micrographs
Autopicking
2,381,498 Particles
2D Classification
1,049,725 particles
Ab-Initio Reconstruction
Heterogeneous Refinement
8%
11%
40%
35%
3%
3%
Non-uniform Refinement
3.32 Å
3.25 Å
Local Refinement
3.88 Å

412

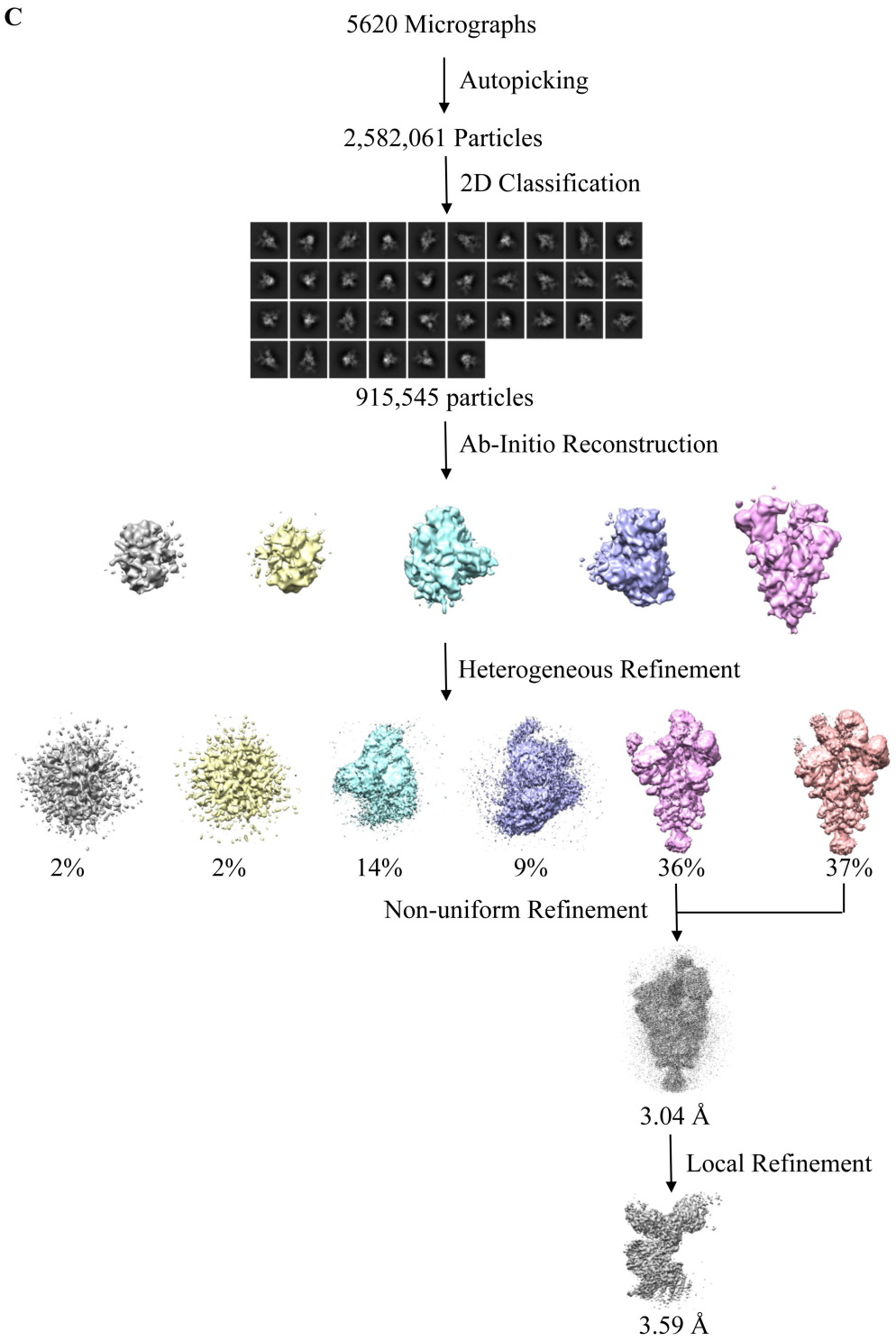

Fig. S2. Cryo-EM data processing workflow. A, Processing workflow of the Spike-F61 binary complex Cryo-EM data. **B,** Processing workflow of the Spike-D2 binary complex Cryo-EM data. **C,** Processing workflow of the Omicron-Spike-F61-D2 ternary complex Cryo-EM data.

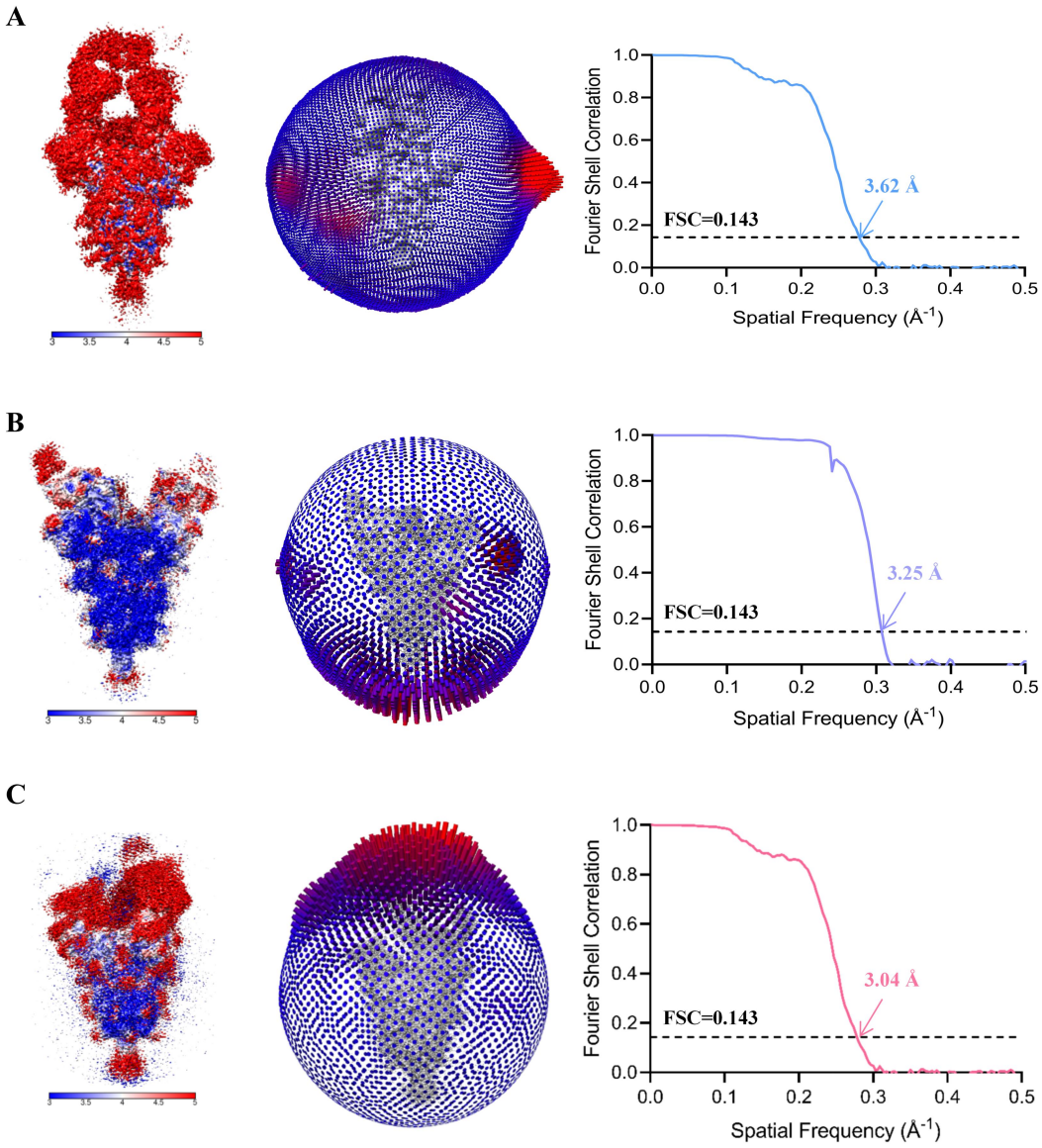

418

419 **Fig. S3. Cryo-EM structure validations. A-C,** Local resolution map (left panel), particle
420 orientation distribution (middle panel) and Gold-standard Fourier Shell Correlation (FSC) curves
421 of the final density maps (right panel) of the Spike-F61 complex (**A**), the Spike-D2 complex (**B**)
422 and the Omicron-Spike-F61-D2 complex (**C**). The final resolution of the Spike-F61 complex is
423 3.62 Å, the final resolution of the Spike-D2 complex is 3.25 Å, and the final resolution of the
424 Omicron-Spike-F61-D2 complex is 3.04 Å.

425

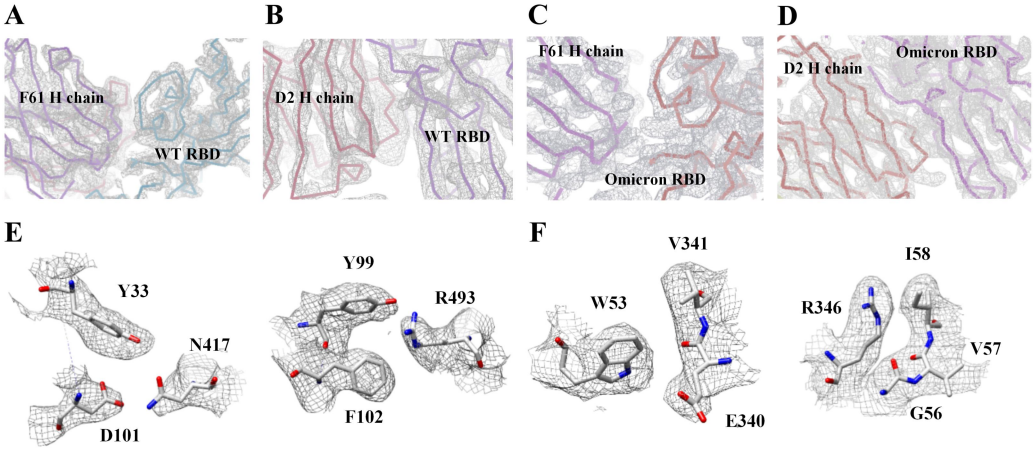

Fig. S4. The representative density maps of residues of the Spike-F61, Spike-D2 and Omicron-Spike-F61-D2 complexes. A, The representative density maps of the WT-RBD-F61 interface. The map is contoured at 2 RMS to show the density. **B,** The representative density maps of the WT-RBD-D2 interface. The map is contoured at 7.2 RMS to show the density. **C,** The representative density maps of the Omicron-RBD-F61 interface. The map is contoured at 5.6 RMS to show the density. **D,** The representative density maps of the Omicron-RBD-D2 interface. The map is contoured at 5.6 RMS to show the density. **E,** The representative density maps of the Omicron-RBD-F61 interacting residues. The map is contoured at 2.2 RMS to show the density. **F,** The representative density maps of the Omicron-RBD-D2 interacting residues. The map is contoured at 2.2 RMS to show the density.

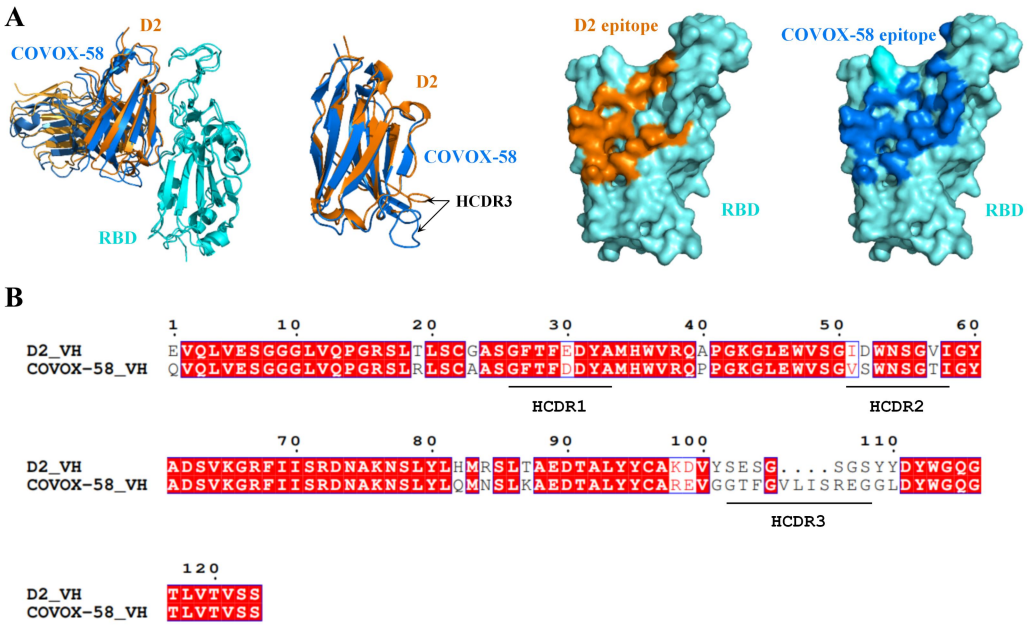

Fig. S5. The comparison of RBD-D2 and RBD-COVOX-58 structures and VH sequences. A, The structural comparison of the RBD-D2 and RBD-COVOX-58 (PDB ID: 7QNY) complexes. These two structures are superimposed to show a similar binding mode and nearly identical epitope. The structure and epitope of COVOX-58 is shown in marine. HCDR3s of D2 and COVOX-58 are indicated with arrows. **B,** Sequence alignment of VH of D2 and COVOX-58.

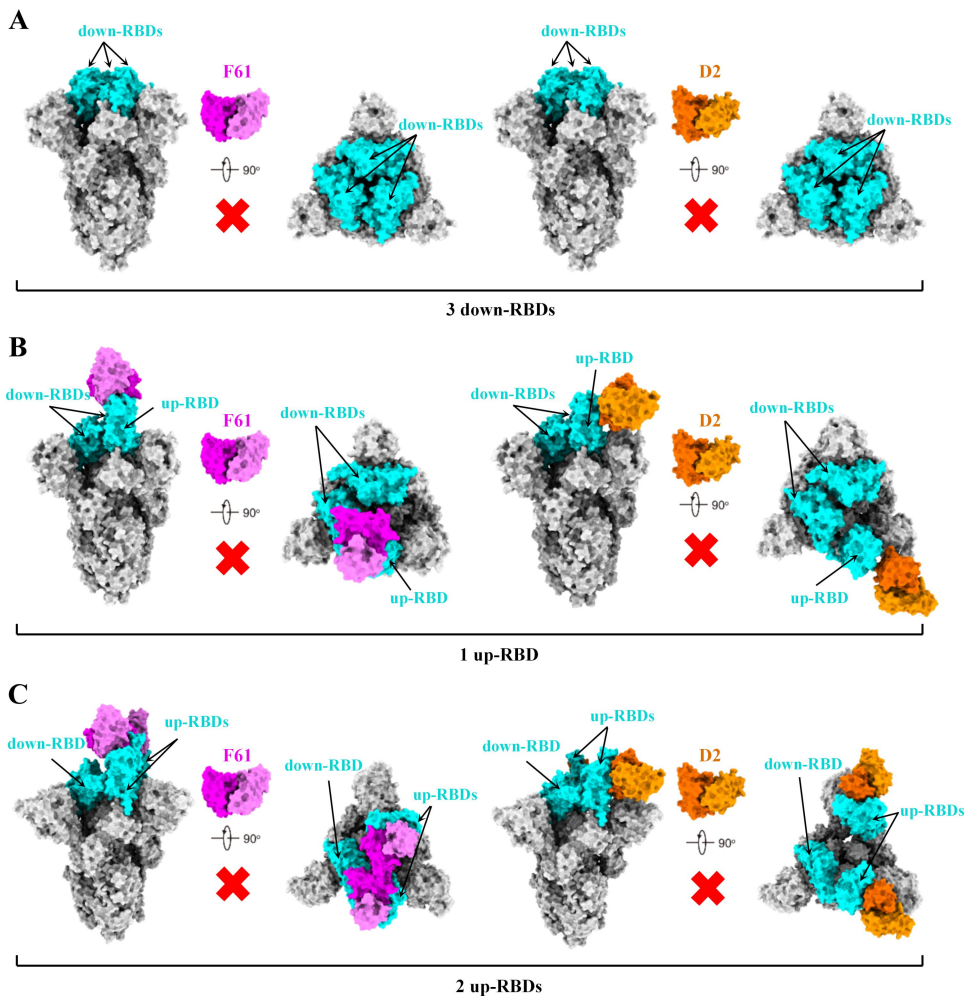

Fig. S6. Alignment of the RBD-F61 or RBD-D2 structures onto the spike trimers in the closed form or in the open form with one or two RBDs adopting the up conformation. A-C, Align RBD-F61 or RBD-D2 complexes to spike trimer with three RBDs in the down conformation (**A**, PDB ID: 6VXX), spike trimer with one RBD in the up conformation (**B**, PDB ID: 6VSB) and spike trimer with two RBDs in the up conformation (**C**, PDB ID: 7A93).

452 **Table S1. Cryo-EM data collection, refinement and validation statistics**

	SARS-CoV-2 spike+F61 fab (EMDB-33307) (PDB-7XMX)	SARS-CoV-2 spike+D2 fab (EMDB-33308) (PDB-7XMZ)	SARS-CoV-2 Omicron spike+F61 Fab+D2 fab (EMDB-33434) (PDB-7XST)
Data collection and processing			
Magnification	29000×	29000×	29000×
Voltage (kV)	300	300	300
Electron exposure (e–/Å^2)	50	50	50
Defocus range (μm)	-1.2 to -1.5	-1.2 to -1.5	-1.2 to -1.5
Pixel size (Å)	0.97	0.97	0.97
Symmetry imposed	C1	C1	C1
Initial particle images (no.)	~820,000	~2,380,000	~2,580,000
Final particle images (no.)	412558	790425	670525
Map resolution (Å)	3.62	3.25	3.04
FSC threshold	0.143	0.143	0.143
Map resolution range (Å)	3.62-6	3.25-6	3.04-6
Refinement			
Initial model used (PDB code)	7KMS	7KMS	7WPF
Model resolution (Å)	3.62	3.25	3.04
FSC threshold	0.143	0.143	0.143
Model resolution range (Å)	3.62	3.25	3.04
Map sharpening *B* factor (Å^2)	-148	-139	-127
Model composition			
Non-hydrogen atoms	29329	29706	33908
Protein residues	3737	3775	4414
Ligands	34	36	37
B factors (Å^2)			
Protein	102.96	70.88	47.73
Ligand	114.89	49.13	59.51
R.m.s. deviations			
Bond lengths (Å)	0.011	0.010	0.006
Bond angles (°)	1.286	1.372	1.315
Validation			
MolProbity score	2.35	2.25	1.86
Clashscore	8.48	9.78	8.86
Poor rotamers (%)	3.46	2.96	0.62
Ramachandran plot			
Favored (%)	92.16	94.46	94.32
Allowed (%)	6.80	5.08	5.61

Disallowed (%)	1.04	0.46	0.07

454 **Table S2. The interacting residues between Fabs and SARS-CoV-2 Omicron Spike**

Complex	RBD	Heavy chain	Light chain
Omicron Spike in complex with F61 fab	R403		N31, N32
	D405		S94
	R408		S97
	T415	S56	
	N417	Y33, D101	
	D420	S56	
	Y421	Y33, Y52, P53, G54	
	Y453	F102	
	L455	Y33, Y99, F102	
	F456	Y33, Y99	
	R457	P53	
	K458	R31, P53	
	N460	G54	
	Y473	R31	
	Q474	R31	
	G476	I28	
	N477	E26, I28	
	K478	E26	
	F486	R97	
	N487	E26, I27, R97	
	Y489	R97	
	R493	Y99, F102	D51
	G502		N31
	G504		N31
	H505		N31
Omicron Spike in complex with D2 fab	E340	W53	
	V341	W53	
	A344	N54	
	T345	E103	
	R346	D52, N54, G56, V57, I58, E103, S104	
	F347	G56	
	A348	N54, S55, G56	
	Y351	I69	
	A352	S55	
	N354	W53, N54	
	K356	W53	
	S446	K65	
	N448	K65	
	Y449	Y60, G66, F68, I69	
	N450	V57, G59	

	L452	I69
	R466	S55, R72
	I468	S71, R72, D73
	T470	H82
	N481	R16
	G482	S17
	F490	I69, R84

A distance cut-off of 4 Å was used.

Materials and Methods

Cells, Viruses and Proteins

Cell lines (HEK293T and Vero E6 cells) were initially acquired from the American Type Culture Collection (ATCC; USA). HEK293T-hACE2-cells were generated via the overexpression of the human ACE2 receptor in HEK293T cells and were used in the neutralization assays of pseudoviruses. Vero E6 cells were used in the neutralization assay of authentic viruses. SARS-CoV-2 WT and variants pseudoviruses were purchased from Beijing Tiantan Pharmaceutical Biotechnology Development Co., Ltd. All SARS-CoV-2 authentic virus were isolated from nasopharyngeal and oropharyngeal samples from patients with COVID-19 and deposited by Wuhan Institute of Biological Products Co., Ltd. Recombinant SARS-CoV-2 proteins, including WT-S1/RBD/NTD (Sino, 40591-V49H\40591-V08H\40592-V02H1), Delta (B.1.617.2) S1/RBD with a his tag (Sino, 40591-V08H23\40592-V08H90), Omicron (BA.1) RBD with a his tag (Sino, 40592-V08H121), Omicron (BA.2) RBD with a his tag (ACRO Biosystems, SPD-C522g) were used in the context of phage-display library panning, binding ELISA or SPR.

Binding ELISA

ELISA plates were coated with SARS-CoV-2 protein including WT-S1, WT-NTD, WT-RBD, Delta-S1, Delta-RBD and Omicron-RBD (Sino Biological, China) at 4 ℃ overnight. Following washing with PBST, serial dilutions of testing antibodies start at 5 μg/mL were added to each well and incubated at 37 ℃ for 30 min. After washing with PBST, horseradish peroxidase (HRP)-conjugated anti-human IgG Fc specific antibody (Sigma, USA) was added at the dilution of 1:2,000 and incubated at 37 ℃ for 30 min. The absorbance was detected at 450 nm. The data were analyzed using GraphPad Prism 8.0.

RBD-ACE2 Binding Inhibition Assayed by FACS

The block assay was assessed by FACS. HEK293T cells were transiently transfected with the ACE2 expression plasmid for 24 h. The mouse-Fc tag Fusion protein of SARS-CoV-2 RBD (RBD-mFC) (Jiangsu East-MabBiomedical Technology, China) at a concentration of 2 μg/mL was mixed with the mAbs or isotype IgG hepatitis b virus (HBV) at a molar ratio of 1:10 and

incubated at 4 ℃ for 1 h. Then mixtures were added to 2.5×10^5 HEK293T cells expressing ACE2 and incubated at 4 ℃ for another hour. Then cells were stained with anti-mouse IgG Taxes red conjugated antibody and anti-human IgG FITC-conjugated antibody (Sigma, USA) for another 30 min then analyzed by FACS Aria II (BD, USA). All of these data were analyzed using Flow Jo.

Antibody Binding Kinetics Measured by SPR

The binding kinetics of mAbs to SARS-CoV-2 Delta-RBD or Omicron-RBD monomer were analyzed using SPR (Biacore 8K; GE Healthcare). Specifically, recombinant protein A (Sino Biological) was immobilized to a CM5 sensor chip. The mAbs (2 μg/mL) were captured by recombinant protein A, and then serial dilutions of SARS-CoV-2 Delta/omicron-RBD with highest concentration of 100 nM to 50 nM were running at a flow rate of 30 μL/min in PBST buffer (1×PBS and 0.05% [vol/vol] Tween-20). The resulting data were fitted to a 1:1 binding model using the Biacore 8K Evaluation software (GE Healthcare). The equilibrium dissociation constants (binding affinity, K_D) for each antibody were calculated using Biacore 8000 Evaluation Software.

Virus Neutralization Assay

The neutralization of authentic SARS-CoV-2 reference strain (GenBank ID: MN996528.1) and variants including Delta B.1.617.2 and Omicron BA.1, BA1.1 and BA.2 were measured by the microneutralization test in the bio-safety Level 3 (BSL-3) laboratory. The assay was performed as described by Manenti et al. with a few modifications[66]. Briefly, two-fold serially diluted antibodies (50 μL) in minimal essential medium (Gibco, Thermo Fisher Scientific, Waltham, MA, USA) supplemented with two percent fetal bovine sera (Gibco, Thermo Fisher Scientific, Waltham, MA, USA) were prepared (four replicates per dilution). In the next step, 50 μL of virus suspension of 100 tissue culture infective dose of previously titrated virus stock was added to each well of a 96 well plate (Greiner bio-one GmbH, Frickenhausen, Germany) and incubated at 37 ℃ for one hour. 100 μL of Vero E6 cells (1×10^5 cells/mL) was then added to the 96 well plates and incubated at 37 ℃ with 5% CO_2. After incubation for 72 h, cytopathic effect (CPE) was observed under a light microscope (Nikon, ×100, Tokyo, Japan). The number of positive holes in each row was counted

515 and the neutralizing titer was calculated using the Reed-Muench method.

516 Neutralization activity of monoclonal antibodies against SARS-CoV-2 pseudoviruses were
517 assayed as previously described[67]. 50 μL serial dilutions of monoclonal antibodies (mAbs) were
518 added into 96-well plates. After that, 50 μL SARS-CoV-2 WT or variants pseudoviruses were
519 incubated with mAbs at 37 ℃ for 1 h. HEK293-hACE2 cells (2.5×10^4 cells/100μL per well)
520 were then added into the mixture and incubated at 37 ℃ in a humidified atmosphere with 5% CO_2
521 for 23 h to 25 h. Then the luciferase activity was measured after cell lysis. The percent of
522 neutralization was determined by comparing with the virus control. The half-maximal inhibitory
523 concentrations (IC50) were determined using 4-parameterlogistic regression (GraphPad Prism
524 version 8).

525

526 **In vivo Protection Activity Evaluation**

527 To evaluate the prophylactic effects of monoclonal antibodies, SARS-CoV-2 Delta and Omicron
528 strains were used in challenge experiments. Male K18-hACE2 mice (6–8 weeks old, purchased
529 from GemPharmatech Co., Ltd. Company.) were randomly distributed into groups (n = 3–6 mice
530 per group). 2 h after administration of monoclonal antibodies, mice were anesthetized with
531 isoflurane and then administered 50 μL SARS-CoV-2 via intranasal route in a challenge dose of
532 100 or 200 $TCID_{50}$/mouse respectively for Delta and Omicron strains. 50 μL of the antibodies at
533 different concentrations (1.25, 2.5, 5 and 20 mg/kg F61, D2 or F61-D2 (ratio of 1:1)) or vehicle
534 (PBS) was administered to each mouse via intranasal route at 2 h before challenge. Mice were
535 monitored every day for body weight changes and clinical signs of disease until all the mice in the
536 control group died. Mice that lost greater than or equal to 25% of their initial body weight were
537 humanely euthanized. At the end point of the experiment, all remaining animals in the monoclonal
538 antibody-administered group received an overdose of isoflurane and were humanely euthanized.
539 Lungs were collected from each mouse postmortem. Tissues were stored at −80 ℃ until further
540 analysis.

541 Tissue homogenates were generated using the TissueLyzer II (Qiagen, Gaithersburg, MD,
542 USA). Briefly, 1000 μL PBS was added to each sample (lungs, 0.01–0.04 g) along with Tungsten
543 carbide 3 mm beads (Qiagen). Samples were homogenized at a speed of 10 Hz for 10 min and

544 then centrifuged at 15,000 × *g* for 10 min. Supernatant was collected, aliquoted, and stored at
545 −80 ℃ until further analysis.
546 Total RNA was extracted from tissues homogenates of lungs using an RNA/DNA
547 Purification Kit (Magnetic Bead) (cat no. DA0623; Daan Gene Co., Ltd., China), and RT-qPCR
548 was performed using a Detection Kit for 2019-nCoV (PCR-Fluorescence) (Fast) (cat no. DA0992;
549 Daan Gene Co., Ltd.) following the manufacturer's instructions. Samples were processed in
550 duplicate using the following cycling protocol: 50 ℃ for 2 min, 95 ℃ for 2 min, followed by 42
551 cycles at 95 ℃ for 5 s and 60 ℃ for 10 s. Viral RNA concentrations (copies/mL) in the lungs of
552 mice were determined using RNA standards for SARS-CoV-2 (Bdsbiotech Co., Ltd., Guangzhou,
553 China). The RT-qPCR results were read according to the Daan Kit criteria, the negative results in
554 this manuscript description mean no signal detected (0 copy) or the CT values of both *N* and
555 *ORF1ab* genes were over 38, corresponding viral RNA copies were under the limitation of the
556 detection (LOD, $10^{2.7}$ copies/mL). All statistical analysis was performed using GraphPad Prism 8.
557 All statistical tests were described in the relevant figure legends.
558
559 **Ethics statement**
560 This study was approved by the Experimental Animal Welfare and Ethical Review Board of
561 Wuhan Institute of Biological Products Co., Ltd (protocol WIBP-AII442021005). The experiments
562 conducted in strict accordance with the recommendations in the Guide for the Care and Use of
563 Laboratory Animals established by the People's Republic of China.
564
565 **Expression and purification of SARS-CoV-2 Spike ectodomain and SARS-CoV-2 Omicron**
566 **Spike ectodomain**
567 The cDNA encoding SARS-CoV-2 WT Spike (GenBank ID: QHD43416.1) was synthesized. Its
568 codons were optimized for insect cell expression and there were six sites mutated to proline. These
569 substitutions occurred at F817, A892, A899, A942, K986 and V987. Furthermore, 'GSAS'
570 substitutions were introduced to residues 682-685, the S1/S2 furin cleavage site. The
571 SARS-CoV-2 Spike ectodomain (1-1208) with a C-terminal Strep tag for purification and a foldon
572 tag for trimerization was inserted into the pFastBac-Dual vector (Invitrogen) and was expressed

573 using Bac-to-Bac baculovirus system (Invitrogen). The constructed recombinant plasmid was
574 transformed into bacterial DH10Bac competent cells, then the extracted bacmid was transfected
575 into Sf9 insect cells using Cellfectin II Reagent (Invitrogen). 7 days later, the baculoviruses were
576 harvested. The low-titre viruses were then used for amplification to generate high-titre
577 baculoviruses, which were used to infect Hi5 insect cells at a density of 2×10^6 cells per ml for
578 protein expression. 60 hours after infection, the supernatant of cell medium containing
579 SARS-CoV-2 Spike was collected and concentrated with buffer changed into Tris buffer (50 mM
580 Tris, pH 8.0, 150 mM NaCl). The SARS-CoV-2 spike ectodomain was purified by Strep-Tactin
581 beads (IBA) and eluted with 10 mM Desthiobiotin in Tris buffer. Then the interest protein was
582 purified by gel-filtration chromatography using a Superose 6 gel filtration column (GE Healthcare)
583 pre-equilibrated with HBS buffer (10 mM HEPES, pH 7.2, 150 mM NaCl). Fractions containing
584 the SARS-CoV-2 Spike ectodomain were collected and concentrated for subsequent electron
585 microscopy analysis.

586 The cDNA encoding SARS-CoV-2 Omicron Spike was synthesized (GenBank ID:
587 ULC25168.1) and cloned into the pCAG vector. There were six sites mutated to proline and these
588 substitutions occurred at F817, A892, A899, A942, K986 and V987. Furthermore, 'GSAS'
589 substitutions were introduced to the S1/S2 furin cleavage site. The SARS-CoV-2 Omicron Spike
590 ectodomain (1-1213) with a C-terminal Strep tag for purification and a foldon tag for trimerization
591 was expressed in FreeStyle 293-F cells (Invitrogen). The plasmid was transiently transfected at a
592 density of 2×10^6 cell per ml using polyethyleneimine (PEI) (Sigma) with a mass ratio of 1:4, and
593 the supernatant was collected 4 days later. The supernatant was concentrated with buffer changed
594 into Tris buffer (50 mM Tris, pH 8.0, 150 mM NaCl). The SARS-CoV-2 Omicron Spike
595 ectodomain was purified by Strep-Tactin beads (IBA) and eluted with 10 mM Desthiobiotin in
596 Tris buffer. Then the protein was purified by gel-filtration chromatography using a Superose 6 gel
597 filtration column (GE Healthcare) pre-equilibrated with HBS buffer (10 mM HEPES, pH 7.2, 150
598 mM NaCl). Fractions containing the SARS-CoV-2 Omicron Spike ectodomain were collected and
599 concentrated for subsequent electron microscopy analysis.

600

601 **Preparation of Fab fragments**

602 F61 and D2 Fab fragments were prepared by digesting F61 and D2 IgG with papain (Sigma),
603 respectively. And then Protein A beads (GenScript) were used to separate Fab fragments,
604 following by gel-filtration chromatography using a Superdex 200 column (GE Healthcare)
605 pre-equilibrated with HBS buffer.
606
607 **Cryo-electron microscopy sample preparation, data collection and processing**
608 The purified SARS-CoV-2 Spike ectodomain was mixed with F61 and D2 Fab with a molar ratio
609 of 1:3, respectively. The purified SARS-CoV-2 Omicron Spike ectodomain was mixed with F61
610 and D2 Fab with a molar ratio of 1:3:3. The final concentrations of the three mixtures were 0.82,
611 1.37 and 0.91 mg/mL in HBS buffer, respectively. Then, Spike trimer - Fab complexes (4 μl) were
612 applied to the pre-glow-discharged holey carbon grids (Quantifoil grid, Cu 300 mesh, R1.2/1.3).
613 The grids were then blotted for 2 seconds with filter paper in 100% relative humidity and 8 °C and
614 plunged into the liquid ethane to freeze samples using FEI Vitrobot system (FEI).
615 Cryo-EM data were collected using FEI Titan Krios (Thermo Fisher Scientific) electron
616 microscope operating at 300 kV with a Gatan K3 Summit direct electron detector (Gatan Inc.) at
617 Tsinghua University. 2905 movies were collected for Spike-F61 complex, 5082 movies were
618 collected for Spike-D2 complex and 5620 movies were collected for Omicron-Spike-F61-D2
619 complex using the SerialEM software[68]. These data were collected at a magnification of 29,000
620 with a pixel size of 0.97 Å and at a defocus range between 1.2-1.5 μm. Each movie had a total
621 accumulate exposure of 50 $e^-/Å^2$ fractionated in 32 frames of 66 ms exposure.
622 MotionCor2 v.1.2.6[69] was used for beam-induced motion correction of whole frames in each
623 movie, and GCTF v.1.18[70] was used to estimate the parameters of contrast transfer function (CTF)
624 for each micrograph. Particles were automatically picked using Gautomatch
625 (http://www.mrc-lmb.cam.ac.uk/kzhang/). And ~820,000 particles for Spike-F61 complex,
626 ~2,380,000 particles for Spike-D2 complex and ~2,580,000 particles for Omicron-Spike-F61-D2
627 complex were extracted using RELION 3.0.8[71], which were used for subsequent 2D classification.
628 Spike-F61 complex used RELION 3.0.8[71] for subsequent data processing. Spike-D2 complex and
629 Omicron-Spike-F61-D2 complex used cryoSPARC[72,73] for subsequent data processing. After one
630 or two rounds of 2D classification, the preferable classes were selected and these selected particles

631 were used to create 3D initial model and perform 3D classification. Finally, a total of 412,558
632 particles for Spike-F61 complex, 790,425 particles for Spike-D2 complex and 670,525 particles
633 for Omicron-Spike-F61-D2 complex were applied to 3D refinement to generate density map and
634 post-processing was performed. Based on the gold-standard Fourier shell correlation (FSC) cutoff
635 of 0.143 criterion, the resolutions were 3.62 Å for Spike-F61 complex, 3.25 Å for Spike-D2
636 complex and 3.04 Å for Omicron-Spike-F61-D2 complex. Local refinement was then performed
637 to further improve the density of the interaction interface of the spike and the Fabs. Local
638 resolution variations were estimated using ResMap 1.1.4[74]. Data collection and processing
639 statistics of Spike-F61 complex, Spike-D2 complex and Omicron-Spike-F61-D2 complex were
640 listed in Table S1.
641
642 **Model building and refinement**
643 The structure of the SARS-CoV-2 Spike in complex with ACE2 with 3-up RBDs (PDB: 7KMS)
644 was used to generate the initial model of Spike for Spike-F61 and Spike-D2 structures, the
645 structure of the SARS-CoV-2 Omicron Spike in complex with JMB2002 with 3-up RBDs (PDB:
646 7WPF) was used to generate the initial model of Omicron Spike for Omicron-Spike-F61-D2
647 structure, and the initial model of Fabs were predicted using AlphaFold2[75]. These atomic models
648 were fit into the final density maps using UCSF Chimera v.1.16[76]. Coot v.0.9.2[77] was subsequently
649 used for manual adjustment and correction according to the protein sequences, map densities,
650 Ramachandran plot, rotamers and bond geometry restraints. The Real Space Refinement of
651 PHENIX v.1.18.2[78] was also used to refine these structures. The quality of the final models was
652 evaluated by PHENIX v.1.18.2[78]. The validation statistics of these structural models were listed in
653 Table 1. Figures were generated using PyMOL 2.0.7[79], UCSF Chimera v.1.16[76], UCSF ChimeraX
654 v.1.13[80].
655

Acknowledgments

We thank the Tsinghua University Branch of China National Center for Protein Sciences (Beijing) for technical support (Cryo-EM, Protein Preparation and Characterization and Biocomputing). This work was supported by funds from the National Key Plan for Scientific Research and Development of China (2021YFC2300104, 2017YFA0205100 and 2021YFC2600200), the National Natural Science Foundation of China (32171202) and Tsinghua University Spring Breeze Fund (2020Z99CFY031).

Author contributions

X.W., X.Y., M.L. and K.D. conceived and designed the study. X.L. carried out protein purification, cryo-EM sample preparation, data collection and processing, model building and refinement with the help of L.Z. and J.Y.. X.L. analyzed the structural data and made related figures. S.S., Y.Q., F.G., J.L. Z.J. and T.H. performed the biochemical experiments and provided original data. Q.Y., L.S. and W.W. analyzed data. Y.P., Z.W., X.S. and J.L. contributed reagents, materials and analysis tools. X.L., D.L., S.W. and L.Z. analyzed and discussed the data. X.L., Q.Y., L.S. and W.W. wrote the manuscript, and X.W., X.Y., M.L. and K.D. edited the manuscript.

Data availability statements

The coordinates of SARS-CoV-2 Spike-F61, SARS-CoV-2 Spike-D2 and SARS-CoV-2 Omicron Spike-F61-D2 have been deposited in the Protein Data Bank (PDB) with the accession numbers 7XMX, 7XMZ and 7XST, respectively; their corresponding maps have been deposited in the Electron Microscopy Data Bank (EMDB) with the accession numbers EMD-33307, EMD-33308 and EMD-33434, respectively.

Competing interests

The authors declare no competing interests.

683 **References**

684 1 Zhou, P. *et al.* A pneumonia outbreak associated with a new coronavirus of probable bat
685 origin. *Nature* **579**, 270-273, doi:10.1038/s41586-020-2012-7 (2020).
686 2 Wu, F. *et al.* A new coronavirus associated with human respiratory disease in China.
687 *Nature* **579**, 265-269, doi:10.1038/s41586-020-2008-3 (2020).
688 3 Zhu, N. *et al.* A Novel Coronavirus from Patients with Pneumonia in China, 2019. *N Engl J*
689 *Med* **382**, 727-733, doi:10.1056/NEJMoa2001017 (2020).
690 4 Cao, Y. *et al.* Potent Neutralizing Antibodies against SARS-CoV-2 Identified by
691 High-Throughput Single-Cell Sequencing of Convalescent Patients' B Cells. *Cell* **182**,
692 73-84 e16, doi:10.1016/j.cell.2020.05.025 (2020).
693 5 Corbett, K. S. *et al.* Evaluation of the mRNA-1273 Vaccine against SARS-CoV-2 in
694 Nonhuman Primates. *N Engl J Med* **383**, 1544-1555, doi:10.1056/NEJMoa2024671
695 (2020).
696 6 Ju, B. *et al.* Human neutralizing antibodies elicited by SARS-CoV-2 infection. *Nature* **584**,
697 115-119, doi:10.1038/s41586-020-2380-z (2020).
698 7 Hansen, J. *et al.* Studies in humanized mice and convalescent humans yield a
699 SARS-CoV-2 antibody cocktail. *Science* **369**, 1010-1014, doi:10.1126/science.abd0827
700 (2020).
701 8 Liu, L. *et al.* Potent neutralizing antibodies against multiple epitopes on SARS-CoV-2
702 spike. *Nature* **584**, 450-456, doi:10.1038/s41586-020-2571-7 (2020).
703 9 Zost, S. J. *et al.* Potently neutralizing and protective human antibodies against
704 SARS-CoV-2. *Nature* **584**, 443-449, doi:10.1038/s41586-020-2548-6 (2020).
705 10 Wu, S. *et al.* A single dose of an adenovirus-vectored vaccine provides protection against
706 SARS-CoV-2 challenge. *Nat Commun* **11**, 4081, doi:10.1038/s41467-020-17972-1
707 (2020).
708 11 Wang, H. *et al.* Development of an Inactivated Vaccine Candidate, BBIBP-CorV, with
709 Potent Protection against SARS-CoV-2. *Cell* **182**, 713-721 e719,
710 doi:10.1016/j.cell.2020.06.008 (2020).
711 12 Vogel, A. B. *et al.* BNT162b vaccines protect rhesus macaques from SARS-CoV-2. *Nature*
712 **592**, 283-289, doi:10.1038/s41586-021-03275-y (2021).
713 13 Robbiani, D. F. *et al.* Convergent antibody responses to SARS-CoV-2 in convalescent
714 individuals. *Nature* **584**, 437-442, doi:10.1038/s41586-020-2456-9 (2020).
715 14 Pinto, D. *et al.* Cross-neutralization of SARS-CoV-2 by a human monoclonal SARS-CoV
716 antibody. *Nature* **583**, 290-295, doi:10.1038/s41586-020-2349-y (2020).
717 15 Baden, L. R. *et al.* Efficacy and Safety of the mRNA-1273 SARS-CoV-2 Vaccine. *N Engl J*
718 *Med* **384**, 403-416, doi:10.1056/NEJMoa2035389 (2021).
719 16 Polack, F. P. *et al.* Safety and Efficacy of the BNT162b2 mRNA Covid-19 Vaccine. *N Engl J*
720 *Med* **383**, 2603-2615, doi:10.1056/NEJMoa2034577 (2020).
721 17 Owen, D. R. *et al.* An oral SARS-CoV-2 M(pro) inhibitor clinical candidate for the
722 treatment of COVID-19. *Science* **374**, 1586-1593, doi:10.1126/science.abl4784 (2021).
723 18 Schafer, A. *et al.* Therapeutic treatment with an oral prodrug of the remdesivir parental
724 nucleoside is protective against SARS-CoV-2 pathogenesis in mice. *Sci Transl Med* **14**,
725 eabm3410, doi:10.1126/scitranslmed.abm3410 (2022).
726 19 Kabinger, F. *et al.* Mechanism of molnupiravir-induced SARS-CoV-2 mutagenesis. *Nat*

Struct Mol Biol **28**, 740-746, doi:10.1038/s41594-021-00651-0 (2021).

20 Taylor, P. C. *et al.* Neutralizing monoclonal antibodies for treatment of COVID-19. *Nat Rev Immunol* **21**, 382-393, doi:10.1038/s41577-021-00542-x (2021).

21 Collier, D. A. *et al.* Sensitivity of SARS-CoV-2 B.1.1.7 to mRNA vaccine-elicited antibodies. *Nature* **593**, 136-141, doi:10.1038/s41586-021-03412-7 (2021).

22 Wang, P. *et al.* Antibody resistance of SARS-CoV-2 variants B.1.351 and B.1.1.7. *Nature* **593**, 130-135, doi:10.1038/s41586-021-03398-2 (2021).

23 Planas, D. *et al.* Reduced sensitivity of SARS-CoV-2 variant Delta to antibody neutralization. *Nature* **596**, 276-280, doi:10.1038/s41586-021-03777-9 (2021).

24 Liu, L. *et al.* Striking antibody evasion manifested by the Omicron variant of SARS-CoV-2. *Nature* **602**, 676-681, doi:10.1038/s41586-021-04388-0 (2022).

25 Challen, R. *et al.* Risk of mortality in patients infected with SARS-CoV-2 variant of concern 202012/1: matched cohort study. *BMJ* **372**, n579, doi:10.1136/bmj.n579 (2021).

26 Kupferschmidt, K. Fast-spreading U.K. virus variant raises alarms. *Science* **371**, 9-10, doi:10.1126/science.371.6524.9 (2021).

27 Tegally, H. *et al.* Sixteen novel lineages of SARS-CoV-2 in South Africa. *Nat Med* **27**, 440-446, doi:10.1038/s41591-021-01255-3 (2021).

28 Fujino, T. *et al.* Novel SARS-CoV-2 Variant in Travelers from Brazil to Japan. *Emerg Infect Dis* **27**, doi:10.3201/eid2704.210138 (2021).

29 Cherian, S. *et al.* SARS-CoV-2 Spike Mutations, L452R, T478K, E484Q and P681R, in the Second Wave of COVID-19 in Maharashtra, India. *Microorganisms* **9**, doi:10.3390/microorganisms9071542 (2021).

30 Mlcochova, P. *et al.* SARS-CoV-2 B.1.617.2 Delta variant replication and immune evasion. *Nature* **599**, 114-119, doi:10.1038/s41586-021-03944-y (2021).

31 Singanayagam, A. *et al.* Community transmission and viral load kinetics of the SARS-CoV-2 delta (B.1.617.2) variant in vaccinated and unvaccinated individuals in the UK: a prospective, longitudinal, cohort study. *Lancet Infect Dis* **22**, 183-195, doi:10.1016/S1473-3099(21)00648-4 (2022).

32 Tao, K. *et al.* The biological and clinical significance of emerging SARS-CoV-2 variants. *Nat Rev Genet* **22**, 757-773, doi:10.1038/s41576-021-00408-x (2021).

33 Karim, S. S. A. & Karim, Q. A. Omicron SARS-CoV-2 variant: a new chapter in the COVID-19 pandemic. *Lancet* **398**, 2126-2128, doi:10.1016/S0140-6736(21)02758-6 (2021).

34 Viana, R. *et al.* Rapid epidemic expansion of the SARS-CoV-2 Omicron variant in southern Africa. *Nature* **603**, 679-686, doi:10.1038/s41586-022-04411-y (2022).

35 Planas, D. *et al.* Considerable escape of SARS-CoV-2 Omicron to antibody neutralization. *Nature* **602**, 671-675, doi:10.1038/s41586-021-04389-z (2022).

36 Callaway, E. Heavily mutated Omicron variant puts scientists on alert. *Nature* **600**, 21, doi:10.1038/d41586-021-03552-w (2021).

37 Kuhlmann, C. *et al.* Breakthrough infections with SARS-CoV-2 omicron despite mRNA vaccine booster dose. *Lancet* **399**, 625-626, doi:10.1016/S0140-6736(22)00090-3 (2022).

38 Tegally, H. *et al.* Continued Emergence and Evolution of Omicron in South Africa: New BA.4 and BA.5 lineages. *medRxiv*, 2022.2005.2001.22274406, doi:10.1101/2022.05.01.22274406 (2022).

39 Wang, Q. H. *et al.* Structural and Functional Basis of SARS-CoV-2 Entry by Using Human ACE2. *Cell* **181**, 894-+, doi:10.1016/j.cell.2020.03.045 (2020).
40 Wrapp, D. *et al.* Cryo-EM structure of the 2019-nCoV spike in the prefusion conformation. *Science* **367**, 1260-1263, doi:10.1126/science.abb2507 (2020).
41 Lan, J. *et al.* Structure of the SARS-CoV-2 spike receptor-binding domain bound to the ACE2 receptor. *Nature* **581**, 215-220, doi:10.1038/s41586-020-2180-5 (2020).
42 Ge, J. *et al.* Antibody neutralization of SARS-CoV-2 through ACE2 receptor mimicry. *Nat Commun* **12**, 250, doi:10.1038/s41467-020-20501-9 (2021).
43 Wang, R. *et al.* Analysis of SARS-CoV-2 variant mutations reveals neutralization escape mechanisms and the ability to use ACE2 receptors from additional species. *Immunity* **54**, 1611-1621 e1615, doi:10.1016/j.immuni.2021.06.003 (2021).
44 Hastie, K. M. *et al.* Defining variant-resistant epitopes targeted by SARS-CoV-2 antibodies: A global consortium study. *Science* **374**, 472-478, doi:10.1126/science.abh2315 (2021).
45 Ferreira, I. *et al.* SARS-CoV-2 B.1.617 Mutations L452R and E484Q Are Not Synergistic for Antibody Evasion. *J Infect Dis* **224**, 989-994, doi:10.1093/infdis/jiab368 (2021).
46 Wrobel, A. G. *et al.* Evolution of the SARS-CoV-2 spike protein in the human host. *Nat Commun* **13**, 1178, doi:10.1038/s41467-022-28768-w (2022).
47 Yin, W. *et al.* Structures of the Omicron spike trimer with ACE2 and an anti-Omicron antibody. *Science* **375**, 1048-1053, doi:10.1126/science.abn8863 (2022).
48 McCallum, M. *et al.* Structural basis of SARS-CoV-2 Omicron immune evasion and receptor engagement. *Science* **375**, 864-868, doi:10.1126/science.abn8652 (2022).
49 Cameroni, E. *et al.* Broadly neutralizing antibodies overcome SARS-CoV-2 Omicron antigenic shift. *Nature* **602**, 664-670, doi:10.1038/s41586-021-04386-2 (2022).
50 Mannar, D. *et al.* SARS-CoV-2 Omicron variant: Antibody evasion and cryo-EM structure of spike protein-ACE2 complex. *Science* **375**, 760-764, doi:10.1126/science.abn7760 (2022).
51 Cele, S. *et al.* Omicron extensively but incompletely escapes Pfizer BNT162b2 neutralization. *Nature* **602**, 654-656, doi:10.1038/s41586-021-04387-1 (2022).
52 Carreno, J. M. *et al.* Activity of convalescent and vaccine serum against SARS-CoV-2 Omicron. *Nature* **602**, 682-688, doi:10.1038/s41586-022-04399-5 (2022).
53 Cao, Y. *et al.* Omicron escapes the majority of existing SARS-CoV-2 neutralizing antibodies. *Nature* **602**, 657-663, doi:10.1038/s41586-021-04385-3 (2022).
54 Zhou, T. *et al.* Structural basis for potent antibody neutralization of SARS-CoV-2 variants including B.1.1.529. *Science* **376**, eabn8897, doi:10.1126/science.abn8897 (2022).
55 VanBlargan, L. A. *et al.* An infectious SARS-CoV-2 B.1.1.529 Omicron virus escapes neutralization by therapeutic monoclonal antibodies. *Nat Med* **28**, 490-495, doi:10.1038/s41591-021-01678-y (2022).
56 Cui, Z. *et al.* Structural and functional characterizations of infectivity and immune evasion of SARS-CoV-2 Omicron. *Cell* **185**, 860-871 e813, doi:10.1016/j.cell.2022.01.019 (2022).
57 Qu, Y. *et al.* Antibody Cocktail Exhibits Broad Neutralization Activity Against SARS-CoV-2 and SARS-CoV-2 Variants. *Virol Sin* **36**, 934-947, doi:10.1007/s12250-021-00409-4 (2021).
58 Lu, J. *et al.* Nasal delivery of broadly neutralizing antibodies protects mice from lethal

challenge with SARS-CoV-2 delta and omicron variants. *Virol Sin*, doi:10.1016/j.virs.2022.02.005 (2022).

59 Walls, A. C. *et al.* Structure, Function, and Antigenicity of the SARS-CoV-2 Spike Glycoprotein. *Cell* **183**, 1735, doi:10.1016/j.cell.2020.11.032 (2020).

60 Benton, D. J. *et al.* Receptor binding and priming of the spike protein of SARS-CoV-2 for membrane fusion. *Nature* **588**, 327-330, doi:10.1038/s41586-020-2772-0 (2020).

61 Dejnirattisai, W. *et al.* SARS-CoV-2 Omicron-B.1.1.529 leads to widespread escape from neutralizing antibody responses. *Cell* **185**, 467-484 e415, doi:10.1016/j.cell.2021.12.046 (2022).

62 Yuan, M. *et al.* Structural basis of a shared antibody response to SARS-CoV-2. *Science* **369**, 1119-1123, doi:10.1126/science.abd2321 (2020).

63 Yuan, M. *et al.* Structural and functional ramifications of antigenic drift in recent SARS-CoV-2 variants. *Science* **373**, 818-823, doi:10.1126/science.abh1139 (2021).

64 Sheward, D. J. *et al.* Structural basis of Omicron neutralization by affinity-matured public antibodies. *bioRxiv*, 2022.2001.2003.474825, doi:10.1101/2022.01.03.474825 (2022).

65 Cao, Y. *et al.* Omicron BA.2 specifically evades broad sarbecovirus neutralizing antibodies. *bioRxiv*, 2022.2002.2007.479349, doi:10.1101/2022.02.07.479349 (2022).

66 Manenti, A. *et al.* Evaluation of SARS-CoV-2 neutralizing antibodies using a CPE-based colorimetric live virus micro-neutralization assay in human serum samples. *J Med Virol* **92**, 2096-2104, doi:10.1002/jmv.25986 (2020).

67 Shan, S. *et al.* A Potent and Protective Human Neutralizing Antibody Against SARS-CoV-2 Variants. *Front Immunol* **12**, 766821, doi:10.3389/fimmu.2021.766821 (2021).

68 Mastronarde, D. N. Automated electron microscope tomography using robust prediction of specimen movements. *Journal of Structural Biology* **152**, 36-51, doi:https://doi.org/10.1016/j.jsb.2005.07.007 (2005).

69 Zheng, S. Q. *et al.* MotionCor2: anisotropic correction of beam-induced motion for improved cryo-electron microscopy. *Nat Methods* **14**, 331-332, doi:10.1038/nmeth.4193 (2017).

70 Zhang, K. Gctf: Real-time CTF determination and correction. *J Struct Biol* **193**, 1-12, doi:10.1016/j.jsb.2015.11.003 (2016).

71 Zivanov, J. *et al.* New tools for automated high-resolution cryo-EM structure determination in RELION-3. *Elife* **7**, doi:10.7554/eLife.42166 (2018).

72 Punjani, A., Rubinstein, J. L., Fleet, D. J. & Brubaker, M. A. cryoSPARC: algorithms for rapid unsupervised cryo-EM structure determination. *Nature Methods* **14**, 290-296, doi:10.1038/nmeth.4169 (2017).

73 Punjani, A., Zhang, H. & Fleet, D. J. Non-uniform refinement: adaptive regularization improves single-particle cryo-EM reconstruction. *Nature Methods* **17**, 1214-1221, doi:10.1038/s41592-020-00990-8 (2020).

74 Kucukelbir, A., Sigworth, F. J. & Tagare, H. D. Quantifying the local resolution of cryo-EM density maps. *Nat Methods* **11**, 63-65, doi:10.1038/nmeth.2727 (2014).

75 Jumper, J. *et al.* Highly accurate protein structure prediction with AlphaFold. *Nature* **596**, 583-589, doi:10.1038/s41586-021-03819-2 (2021).

76 Pettersen, E. F. *et al.* UCSF Chimera--a visualization system for exploratory research and

analysis. *J Comput Chem* **25**, 1605-1612, doi:10.1002/jcc.20084 (2004).

77 Emsley, P. & Cowtan, K. Coot: model-building tools for molecular graphics. *Acta Crystallogr D* **60**, 2126-2132, doi:10.1107/S0907444904019158 (2004).

78 Adams, P. D. *et al.* PHENIX: a comprehensive Python-based system for macromolecular structure solution. *Acta Crystallogr D Biol Crystallogr* **66**, 213-221, doi:10.1107/S0907444909052925 (2010).

79 Janson, G., Zhang, C., Prado, M. G. & Paiardini, A. PyMod 2.0: improvements in protein sequence-structure analysis and homology modeling within PyMOL. *Bioinformatics* **33**, 444-446, doi:10.1093/bioinformatics/btw638 (2017).

80 Pettersen, E. F. *et al.* UCSF ChimeraX: Structure visualization for researchers, educators, and developers. *Protein Sci* **30**, 70-82, doi:10.1002/pro.3943 (2021).